

# Deep Learning for Multiscale Damage Analysis via Physics-Informed Recurrent Neural Network

Shiguang Deng<sup>1</sup>, Shirin Hosseinmardi<sup>2</sup>, Diran Apelian<sup>1</sup>, and Ramin Bostanabad\*<sup>2</sup>

<sup>1</sup>ACRC, Materials Science and Engineering, University of California, Irvine

<sup>2</sup>Department of Mechanical and Aerospace Engineering, University of California, Irvine

## Abstract

Direct numerical simulation of hierarchical materials via homogenization-based concurrent multiscale models poses critical challenges for 3D large scale engineering applications, as the computation of highly nonlinear and path-dependent material constitutive responses at the lower scale causes prohibitively high computational costs. In this work, we propose a physics-informed data-driven deep learning model as an efficient surrogate to emulate the effective responses of heterogeneous microstructures under irreversible elasto-plastic hardening and softening deformation. Our contribution contains several major innovations. First, we propose a novel training scheme to generate arbitrary loading sequences in the sampling space confined by deformation constraints where the simulation cost of homogenizing microstructural responses per sequence is dramatically reduced via mechanistic reduced-order models. Second, we develop a new sequential learner that incorporates thermodynamics consistent physics constraints by customizing training loss function and data flow architecture. We additionally demonstrate the integration of trained surrogate within the framework of classic multiscale finite element solver. Our numerical experiments indicate that our model shows a significant accuracy improvement over pure data-driven emulator and a dramatic efficiency boost than reduced models. We believe our data-driven model provides a computationally efficient and mechanics consistent alternative for classic constitutive laws beneficial for potential high-throughput simulations that needs material homogenization of irreversible behaviors.

**Keywords:** Deep learning; recurrent neural network; data-driven surrogate; physics constraints; elasto-plasticity; multiscale modeling

## 1 Introduction

Heterogeneous materials are increasingly utilized in support structures in many engineering applications. Analyzing their intricate material behaviors often resorts to multiscale models, FE<sup>2</sup> as a homogenization-based concurrent multiscale model being one of the most popular approaches. Despite computational power growth and mechanics theory advancement in recent years, the simulation of hierarchical materials via FE<sup>2</sup> still causes prohibitively

---

\*Corresponding Author: Raminb@uci.edu

high computational costs. Consider the multiscale model in Figure 1 where each integration point (IP) of the macroscale component is associated with a microstructure of complex local morphology. Massive spatial discretization at both scales results in not only significant computer memory storage but also long computational time as the simulation iterates through each microstructure. It is therefore evident that the computational bottleneck of multiscale simulations lies in the evaluation of microstructural responses. To address such bottleneck, we propose a memory-light and computationally efficient deep learning model to emulate the microstructural analyses in multiscale scenarios.

Considering as an efficient alternative to  $FE^2$ , mechanistic reduced-order models (ROM) have seen a boom in the late decade. Its main idea is to strike a balance between simulation accuracy and efficiency through various hyper reduction techniques to reduce the number of unknown variables from solution systems. For example, transformed field analysis method [1] and its non-uniform variant [2] employ proper orthogonal decomposition technique to reduce material state variables by expressing arbitrary strain fields as a subspace representation of pre-computed eigenstrains. Clustering-based ROM see a rapid development in recent years which reduces unknown variables by agglomerating a large number of material points into a few clusters. For instance, the self-consistent clustering [3] and its later variant, the virtual clustering analysis [4], by assuming material points in a cluster exhibiting close elastic responses should also behave similarly for inelastic deformations, solve incremental Lippmann-Schwinger equations to approximate the evolution of cluster-wise material responses. Recently, a deflated clustering analysis [5] utilizes clusters to decompose both macroscale and microscale domains where macro analysis is faithfully accelerated in a deflation space while the effective microstructural responses are approximated in a coarse-graining manner that close-by material points are assumed to share the same behaviors. Its robustness and efficiency are further improved in a later work [6] where both spatial and temporal dimensions are adaptively reduced for elasto-plastic softening simulations. In spite of dramatic efficiency improvement, the representation capability of ROM is often limited, especially for modeling strain localization phenomena where insufficient number of local clusters lead to artificially strengthened material responses in diffusive solutions. Additionally, since reduced-order micro analysis needs to be performed along with multiscale simulations, ROM still requires a considerable amount of computer memory storage that is often only available on high performance computer clusters, limiting its accessibility. More importantly, ROM, being a mechanistic model, lacks solution transferability, as the expensive simulation data of one model is not applicable to others.

Data-driven surrogate is another type of viable alternative capable of data transferability to emulate the direct numerical multiscale simulations. Among various types of machine learning models, recurrent neural network (RNN) is adopted by many recent publications to approximate the history-dependent material constitutive laws. This is because RNN, which makes use of sequential information to correlate sequences of input and output data, is equipped with hidden variables as the model memory to track input's history. For example, in the work [7] by Mozaffar et al., a RNN model is demonstrated capable of accurate prediction of material plasticity with distortional hardening on 2D composite microstructures. Wang et al. [8] developed a RNN framework to link information from different scales via recursive homogenization to capture the multiscale hydro-mechanical coupling effects of

heterogeneous media with various sizes of pores. The RNN model developed by Wu et al. [9] is trained on a database whose sampling sequences are generated via a random walking algorithm to simulate the microstructural effective elasto-plastic hardening behaviors under cyclic and non-proportional loading paths. An on-demand sampling strategy is adopted by Ghavamian et al. [10] that reduces sampling space by running prior macro models to collect the strain-stress sequences for the subsequent RNN’s learning process. This strategy reduces sampling efforts and improves prediction accuracy, nevertheless, resulting in limited generality since the trained model can be only applied to the same macro component which the training sequences are collected from. In a recent work [11], Logarzo et al. uses RNN to develop a smart constitutive law that regulates the plastic hardening behaviors of a 2D composite microstructure under versatile deformation histories sampled from the space of principal strains. All aforementioned surrogates are black-box or pure data-driven models. Such models are proven highly accurate on the condition of abundant training dataset; however, since they lack physics information, their emulated solutions may exhibit mechanistic inconsistency and lack engineering interpretation.

Our contribution of this work is to propose a physics-constrained RNN to emulate the micro analyses amid online multiscale simulations. Comparing to the aforementioned ROM and pure data-driven models, our proposed surrogate is computationally efficient, memory light, physics consistent and transferable. Our surrogate is developed in an offline stage, and it consists of three major components as shown in Figure 1:

- **Microstructure representation.** The essence of data transferability of our model comes from the generality of versatile deformation paths our microstructures are deformed by. To maximize the diversity of our sequential dataset, we utilize design of experiment (DoE) method to generate a set of random 3D deformation histories with six independent strain components over a series of time steps.
- **Response database generation.** Emulating 3D large scale microstructural responses faces two major challenges. The first challenge comes from the prohibitively high dimensions of the functional space representing sequential data, and the second challenge is the demanding computational costs pertaining to the softening simulation per deformation path in the sampling space. To address such difficulties, we generate a moderate size of response training database by adopting DoE constraints to remove unnecessary sampling sequences, and we deploy mechanistic ROM to faithfully and efficiently compute the microstructural responses where softening-induced solver divergence is addressed by hybrid time integration scheme.
- **Surrogate development.** To improve the accuracy of our surrogate whose training lacks abundant sequential data, we develop and incorporate thermodynamics consistent physics constraints within our RNN by modifying loss function and data flow architecture. By integrating our trained surrogate in the Newton Raphson algorithm, our model is able to provide highly accurate iterative emulations towards convergence at each loading step in online multiscale simulations.

Our paper is organized as follows. In Section 2, we briefly review the homogenization-based concurrent multiscale damage analysis along with the numerical techniques for convergent

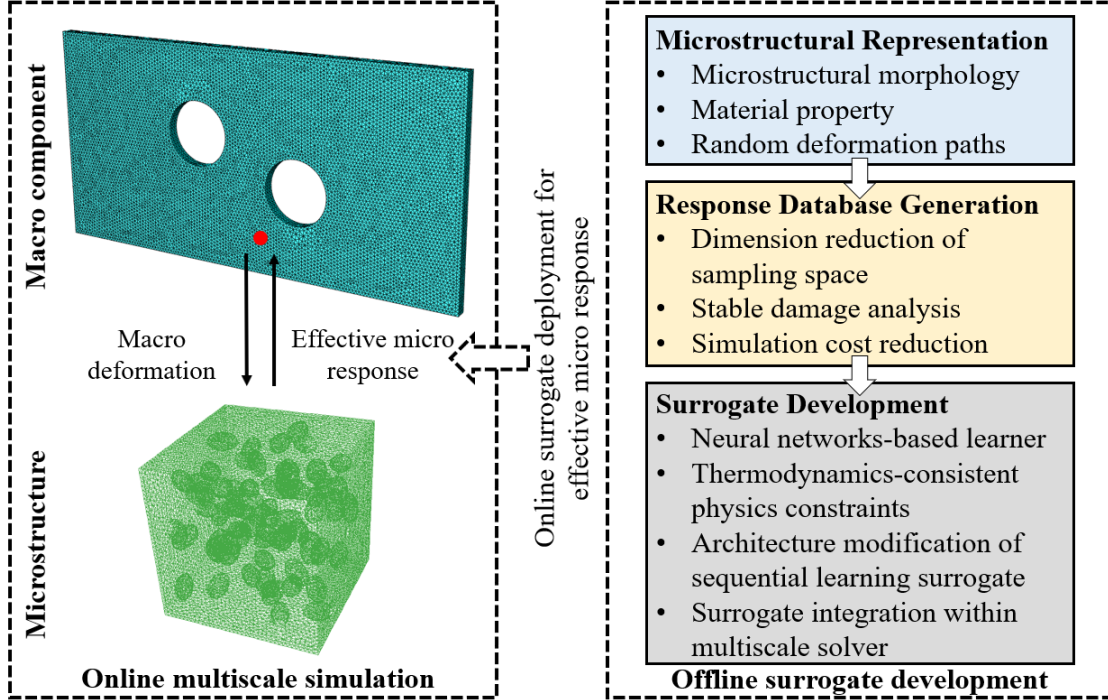


**Figure 1 Framework of the proposed data-driven material model:** Our physics-informed data-driven model, emulating the microstructural effective responses amid online multiscale simulations, is composed of three major offline components: microstructural representation, response database generation and surrogate model development.

softening simulations. We also demonstrate two thermodynamics-consistent physics constraints that a generic microstructure should always satisfy under arbitrary deformations. In Section 3, we propose our physics-informed data-driven model for the emulation of microstructural effective elasto-plastic responses. In Section 4, We proceed to illustrate the efficiency and accuracy of our model by comparing its prediction not only to the microstructural effective responses subject to random deformation paths, but also on a number of multiscale structures which are subject to complex cyclic loading conditions with hardening and softening material behaviors. In the end, we conclude our paper with summary and future work in Section 5.

## 2 Homogenization-based multiscale damage analysis

In this section, we start to review the first-order homogenization-based multiscale simulations in Section 2.1. We then present the strain softening model for damage evolution and a hybrid time integration scheme to address its numerical instability in Section 2.2 and Section 2.3, respectively. We proceed to perform a thermodynamics-consistent energy analysis in Section 2.4 to demonstrate the constraints for an arbitrary RVE that is subject to generic iso-thermal elasto-plastic deformation paths.

### 2.1 Multiscale modeling

Our multiscale models in this work are based on the first-order computational homogenization method which assumes scale separation between macro-components and micro-features. In solving multiscale systems, the solutions at the macroscale and microscale are coupled via the Hill-Mandel condition [12] that indicates the density of virtual internal work of a

macroscale IP equals to the volume average of the virtual work in the associated microstructure subject to any kinematically admissible displacement field as:

$$\mathbf{S}_M : \delta \mathbf{E}_M = \frac{1}{|\Omega_{0m}|} \int_{\Omega_{0m}} \mathbf{S}_m : \delta \mathbf{E}_m d\Omega \quad (1)$$

where  $\mathbf{S}_M$ ,  $\delta \mathbf{E}_M$ ,  $\mathbf{S}_m$  and  $\delta \mathbf{E}_m$  represent the macroscopic and microscopic stress and virtual strain tensors, respectively. The subscripts  $M$  and  $m$  indicate the macroscale and microscale, respectively. The  $:$  operator represents the double dot product contracting a pair of repeated indices. In addition,  $\Omega_{0m}$  and  $|\Omega_{0m}|$  indicate the reference microstructural domain and its volume, respectively. Following the virtual energy condition, the macroscopic effective stress and virtual strain can be expressed as the volume average of their micro-counterparts as:

$$\mathbf{S}_M = \frac{1}{|\Omega_{0m}|} \int_{\Omega_{0m}} \mathbf{S}_m d\Omega; \quad \delta \mathbf{E}_M = \frac{1}{|\Omega_{0m}|} \int_{\Omega_{0m}} \delta \mathbf{E}_m d\Omega \quad (2)$$

The stress and strain fields at both the macro- and micro- scales need to satisfy equilibrium equations at their length scale. For instance, under the infinitesimal deformation assumption, the macro-solutions at an arbitrary macroscopic point  $\mathbf{P}$  can be computed by solving a set of equilibrium equations in a boundary value problem (BVP) as:

$$\mathbf{S}_M(\mathbf{P}) \cdot \nabla_0 + \mathbf{b}_M = \mathbf{0} \quad \forall \mathbf{P} \in \Omega_{0M} \quad (3a)$$

$$\mathbf{u}_M(\mathbf{P}) = \bar{\mathbf{u}}_M \quad \forall \mathbf{P} \in \Gamma_{0M}^D \quad (3b)$$

$$\mathbf{S}_M(\mathbf{P}) \cdot \mathbf{n}_M = \bar{\mathbf{t}}_M \quad \forall \mathbf{P} \in \Gamma_{0M}^N \quad (3c)$$

where  $\mathbf{u}_M$  and  $\bar{\mathbf{u}}_M$  are the unknown macroscopic displacement and prescribed displacement on the Dirichlet boundary  $\Gamma_{0M}^D$  over the undeformed macroscopic domain  $\Omega_{0M}$  with an outward unit vector  $\mathbf{n}_M$ . Also,  $\nabla_0$  indicates the gradient operator with respect to the original configuration.  $\mathbf{b}_M$  and  $\bar{\mathbf{t}}_M$  represent the body force and prescribed surface traction on the Neumann boundary  $\Gamma_{0M}^N$ , respectively. In a similar manner, the strong form of the microscale equilibrium equations can be written as a BVP for the microstructure or representative volume element (RVE) composed of micro-points  $\mathbf{p}$  as:

$$\mathbf{S}_m(\mathbf{p}) \cdot \nabla_0 = \mathbf{0} \quad \forall \mathbf{p} \in \Omega_{0m} \quad (4a)$$

$$\mathbf{S}_m(\mathbf{p}) \cdot \mathbf{n}_m = \bar{\mathbf{t}}_m \quad \forall \mathbf{p} \in \Gamma_{0m} \quad (4b)$$

where  $\bar{\mathbf{t}}_m$  indicates the surface traction per unit area over the reference microstructural boundary  $\Gamma_{0m}$  with an outward unit normal vector  $\mathbf{n}_m$ .

## 2.2 Strain softening

In this work, we adopt isotropic continuum damage model to simulate the strain softening in ductile metals whose load-carrying capacity drops as a consequence of the degradation of yield stress and stiffness. To simulate the onset of softening, we choose ductile damage initiation criteria which assumes the effective strain  $\bar{E}_d^{pl}$  at damage initiation as a function of stress states and strain rates. For the sake of simplicity, we presume  $\bar{E}_d^{pl}$  as a constant and assume damage begins simply when the equivalent plastic strain is equal or greater than the damage initiation criteria, i.e.,  $\bar{E}^{pl} \geq \bar{E}_d^{pl}$ .

Softening continues to progress after damage initiation. We can write the constitutive equations of a progressing damage state in a ductile metal with elasto-plastic behaviors as:

$$\mathbf{S} = (1 - D)\mathbf{S}^0; \quad \mathbf{S}^0 = \mathbb{C}^{el} : \mathbf{E}^{el} = \mathbb{C}^{el} : (\mathbf{E} - \mathbf{E}^{pl}) \quad (5)$$

where  $\mathbf{S}$  and  $\mathbf{S}^0$  are the damaged stress and the reference stress that undergoes the same deformation path but in the absence of damage, respectively.  $\mathbb{C}^{el}$  represents the fourth-order elasticity tensor.  $\mathbf{E}$ ,  $\mathbf{E}^{el}$  and  $\mathbf{E}^{pl}$  are the total strain, elastic strain and plastic strain vectors, respectively.  $D$  represents the damage parameter that monotonically increases within  $[0, 1]$ . We note that in our context of isotropic continuum damage,  $D$  is a scalar and it becomes a tensor in anisotropic damage models.

A major challenge of using the isotropic continuum damage model in Equation 5 is the softening-induced non-positive stiffness matrix that results in solution convergence issues and negative wave speeds [13]. Specifically, the ill-posed problem causes equilibrium equations to lose objectivity with respect to mesh sizes by exhibiting spurious mesh sensitivity. We therefore adopt two different damage models to mitigate the mesh dependency at macroscale and microscale, respectively.

For macroscopic softening, we define the evolution of damage parameter  $D_M$  as a function of  $\bar{E}^{pl}$ ,  $\bar{E}_d^{pl}$ , and an evolution rate parameter  $\alpha$  as [14]:

$$D_M(\bar{E}^{pl}, \alpha) = 1 - \frac{\bar{E}_d^{pl}}{\bar{E}^{pl}} \exp(-\alpha(\bar{E}^{pl} - \bar{E}_d^{pl})) \quad (6)$$

where  $\alpha$  is a user-defined non-negative value. The definition of Equation 6 ensures that when  $D_M$  increases to 1.0 as the  $\bar{E}^{pl}$  is sufficiently larger than  $\bar{E}_d^{pl}$ , damage results in rupture with fully degraded modulus. We then constrain the progression of  $D_M$  by an integral-type non-local damage model to mitigate the spurious mesh dependency as:

$$\hat{D}_M(\mathbf{P}, \mathbf{P}') = \int_B \omega(\|\mathbf{P} - \mathbf{P}'\|) D_M(\mathbf{P}') d\mathbf{P}' \quad (7)$$

where  $\hat{D}_M(\mathbf{P}, \mathbf{P}')$  is the non-local damage parameter at a macroscopic point  $\mathbf{P}$  surrounded by close-by points  $\mathbf{P}'$  in a compact neighborhood  $B$ .  $D_M(\mathbf{P}')$  represents the local damage parameter at  $\mathbf{P}'$ , and  $\omega$  indicates the non-local weighting function depending on the distance  $\|\mathbf{P} - \mathbf{P}'\|$  between the studied point and its supporting points. In this work, We define  $\omega$  by a polynomial bell-shape function as:

$$\omega(\|\mathbf{P} - \mathbf{P}'\|) = \frac{\omega_\infty(\|\mathbf{P} - \mathbf{P}'\|)}{\int_B \omega_\infty(\|\mathbf{P} - \mathbf{P}'\|) d\mathbf{P}'}; \quad \omega_\infty(\|\mathbf{P} - \mathbf{P}'\|) = \left\langle 1 - \frac{4(\|\mathbf{P} - \mathbf{P}'\|)^2}{l_d^2} \right\rangle^2 \quad (8)$$

where  $\langle \dots \rangle$  is the Macauley bracket defined as  $\langle x \rangle = \max(0, x)$ .  $l_d$  denotes the strain localization bandwidth whose value represents the non-local interacting radius, and the support domain  $B$  is a sphere with a radius of  $l_d/2$  in 3D models.

To address the lack of objectivity to mesh choices in microstructural damage simulations, re-definition of a microscopic strain localization bandwidth would counteract the physical

meaning of its macroscopic counterpart  $l_d$ . Instead, we convert the microstructural softening constitutive equation from stress-strain relation to the stress-displacement relation to drive the micro-damage evolution after initiation as:

$$G_f = \int_{\bar{E}_0^{pl}}^{\bar{E}_f^{pl}} l_e S_y d\bar{E}^{pl} = \int_0^{\bar{u}_f^{pl}} S_y d\bar{u}^{pl} \quad (9)$$

where  $l_e$  indicates the element characteristic length in an arbitrary RVE,  $G_f$  represents the dissipated energy after damage initiation that opens a unit area of crack. The equivalent plastic displacement  $\bar{u}^{pl}$  is the fracture work conjugate to the yield stress  $S_y$  in the fracture evolution from the damage initiation (with the effective plastic strain  $\bar{E}_0^{pl}$  and zero plastic displacement  $\bar{u}^{pl}$ ) to the final failure (with the effective fracture strain  $\bar{E}_f^{pl}$  and the fracture displacement  $\bar{u}_f^{pl}$ ). We can then define the damage evolution rule based on the amount of released energy in an exponential form of the plastic displacement [15] as in Equation 10. We note that  $D_m$  approaches 1.0 asymptotically with infinitely large  $\bar{u}^{pl}$ . In practice, we set  $D_m$  as 1.0 when the dissipated energy exceeds  $0.99G_f$ .

$$D_m = 1 - \exp\left(-\frac{1}{G_f} \int_0^{\bar{u}_f^{pl}} S_y d\bar{u}^{pl}\right) \quad (10)$$

### 2.3 Hybrid temporal integration

The underlying reason of the convergence difficulty in continuum damage simulations via classic implicit time integration scheme comes from the non-positive stiffness matrix of governing equations. For illustration, consider the constitutive equation of an isotropic damage model integrated by an implicit backward-Euler integration scheme. Its algorithmic tangent operator at an arbitrary IP can be written as:

$$\mathbb{C}_{n+1}^{alg} = \frac{\partial \mathbf{S}_{n+1}}{\partial \mathbf{E}_{n+1}} = (1 - D_{n+1})\mathbb{C}^{el} - \frac{S_{n+1} - H_n \bar{E}_{n+1}^{pl}}{(\bar{E}_{n+1}^{pl})^3} \mathbf{S}_{n+1}^0 \otimes \mathbf{S}_{n+1}^0 \quad (11)$$

where  $\mathbb{C}_{n+1}^{alg}$ ,  $\bar{E}_{n+1}^{pl}$ ,  $S_{n+1}$ ,  $\mathbf{S}_{n+1}^0$  and  $H_n$  represent the fourth-order algorithmic tangent operator, equivalent plastic strain, equivalent stress, referenced stress tensor, and softening modulus, respectively. The subscripts indicate the indices of time steps, and the symbol  $\otimes$  represents the cross product between tensors. Softening causes negative values of  $H_n$  that can result in the loss of positiveness in  $\mathbb{C}_{n+1}^{alg}$ . Non-positive  $\mathbb{C}_{n+1}^{alg}$  leads to ill-conditioned elemental stiffness matrix with near-zero or negative eigenvalues, and further deteriorates the global stiffness matrix through element assembly process. Such ill-posed problem dramatically affects the efficiency of iterative solvers, e.g., Newton-Raphson methods, and often causes job abortion before final convergence.

To fundamentally resolve the convergence issue, we adopt a hybrid time integration scheme [6, 16] in our work to integrate the governing equations of elasto-plastic and softening equations explicitly-and-implicitly which results in much improved convergence performance.

The basic idea of the hybrid integration is to maintain the positive-definiteness of the system's algebraic tangent operator by separately integrating constitutive equations in two

consecutive steps via explicit and implicit schemes, respectively. In the first step, choice of internal material state variables at time step  $n + 1$  are explicitly extrapolated from the previous step  $n$  to compute an explicit stress state  $\tilde{\mathbf{S}}_{n+1}$  that balances the equilibrium equation between internal and external forces. In the second step, we compute an implicit stress state  $\mathbf{S}_{n+1}$  based on the current strain state  $\mathbf{E}_{n+1}$  through the classic backward Euler method. The computed implicit stress  $\mathbf{S}_{n+1}$  then updates trial stress and yield function in the next time step  $n + 2$ .

For elasto-plastic model, we choose the material state variable as the incremental plastic strain tensor  $\Delta\tilde{\mathbf{E}}_{n+1}^{pl}$  such that the explicitly extrapolated stress  $\tilde{\mathbf{S}}_{n+1}$  can be computed as:

$$\begin{aligned}\tilde{\mathbf{S}}_{n+1}(\Delta\tilde{\mathbf{E}}_{n+1}^{pl}) &= \tilde{\mathbf{S}}_{n+1}^{trial} - \mathbb{C}^{el} : \Delta\tilde{\mathbf{E}}_{n+1}^{pl} = \mathbb{C}^{el} : \mathbf{E}_{n+1} - \mathbb{C}^{el} : \mathbf{E}_n^{pl} - \mathbb{C}^{el} : \Delta\tilde{\mathbf{E}}_{n+1}^{pl} \\ \Delta\tilde{\mathbf{E}}_{n+1}^{pl} &= \frac{\Delta t_{n+1}}{\Delta t_n} \Delta\mathbf{E}_n^{pl}\end{aligned}\quad (12)$$

where  $\mathbf{E}_n^{pl}$  represents the implicit incremental plastic strain tensor from the last time step  $n$ ,  $\Delta t_n$  and  $\Delta t_{n+1}$  indicate the lengths of time steps at the two consecutive steps. The algorithmic tangent operator under loading scenarios is therefore computed as:

$$\tilde{\mathbb{C}}_{n+1}^{alg} = \frac{\partial\tilde{\mathbf{S}}_{n+1}(\Delta\tilde{\mathbf{E}}_{n+1}^{pl})}{\partial\mathbf{E}_{n+1}} = \frac{\partial(\mathbb{C}^{el} : \mathbf{E}_{n+1} - \mathbb{C}^{el} : \mathbf{E}_n^{pl} - \mathbb{C}^{el} : \Delta\tilde{\mathbf{E}}_{n+1}^{pl})}{\partial\mathbf{E}_{n+1}} = \mathbb{C}^{el} \quad (13)$$

In similar manner, for isotropic continuum damage models, we can choose the explicitly interpolated material state variable in the hybrid integration as the incremental plastic multiplier  $\Delta\tilde{\lambda}_{n+1}$ , i.e.,  $\Delta\tilde{\lambda}_{n+1} = (\Delta t_{n+1}/\Delta t_n)\Delta\lambda_n$ . We can then write its explicit damaged stress and algorithmic tangent operator under loading conditions as:

$$\tilde{\mathbf{S}}_{n+1} = (1 - \tilde{D}_{n+1})\mathbf{S}_{n+1}^0 = (1 - \tilde{D}_{n+1})\mathbb{C}^{el} : \mathbf{E}_{n+1}; \quad \tilde{D}_{n+1} = \tilde{D}_{n+1}(D_n, \Delta\tilde{\lambda}_{n+1}) \quad (14)$$

$$\tilde{\mathbb{C}}_{n+1}^{alg} = \frac{\partial\tilde{\mathbf{S}}_{n+1}}{\partial\mathbf{E}_{n+1}} = (1 - \tilde{D}_{n+1})\mathbb{C}^{el} \quad (15)$$

where  $\mathbf{S}_{n+1}^0$  is the effective stress tensor, and  $\tilde{D}_{n+1}$  represents the explicit state of the damage variable which is a function of its previous implicit state  $D_n$  and the current explicit incremental plastic multiplier  $\Delta\tilde{\lambda}_{n+1}$ . We note that in the hybrid integration scheme, the unloading tangent operators of the elasto-plastic model in Equation 13 and the damage model in Equation 15 are trivially equal to the elastic modulus  $\mathbb{C}^{el}$ . Hence, the hybrid integration scheme is not only advantageous in preserving the positive-definiteness of the governing equations, but also letting the global stiffness matrix be assembled only once before online simulations. The global stiffness stays constant for the elasto-plastic analysis and only needs partial update on matrix entries associated to softening IPs. As softening is often highly localized in small regions, the global stiffness can be incrementally updated during the whole elasto-plastic-softening process [6], saving significant memory footprints with robust convergence performance.

## 2.4 Energy analysis

Assume a microscopic material point in an RVE is subject to an iso-thermal elasto-plastic deformation. We can compute its total work rate per unit volume  $\hat{W}$  via thermodynamics



principles [17] as:

$$\hat{W} = \dot{\psi} + \Phi \quad (16)$$

where  $\dot{\psi}$  represents the rate of Helmholtz free energy, and  $\Phi$  accounts for the rate of dissipated energy including the dissipation from plasticity, damage, damping, etc. For general elasto-plastic material behaviors, the rate of work can be decomposed into an elastic and a plastic parts as:

$$\hat{W} = \hat{W}^{el} + \hat{W}^{pl} \quad (17)$$

where the elastic work rate  $\hat{W}^{el}$  at an arbitrary micro-point is equal to the rate of recoverable elastic free energy or strain energy  $\dot{\psi}^{el}$ , while the plastic work rate  $\hat{W}^{pl}$  is equal to the sum of the conditionally recoverable plastic free energy  $\dot{\psi}^{pl}$  and the irrecoverable dissipation rate  $\Phi$  [18] as:

$$\hat{W}^{el} = \dot{\psi}^{el} = \mathbf{S}_m : \dot{\mathbf{E}}_m^{el}; \quad \hat{W}^{pl} = \dot{\psi}^{pl} + \Phi = \mathbf{S}_m : \dot{\mathbf{E}}_m^{pl} \quad (18)$$

The total rate of work per unit volume  $\hat{W}$  of the RVE can be therefore written as the multiplication of the micro-stress  $\mathbf{S}_m$  and the rate of microscopic total strain  $\dot{\mathbf{E}}_m$  by assuming an additive decomposition rule of the strain as:

$$\hat{W} = \mathbf{S}_m : \dot{\mathbf{E}}_m^{el} + \mathbf{S}_m : \dot{\mathbf{E}}_m^{pl} = \mathbf{S}_m : \dot{\mathbf{E}}_m \quad (19)$$

Based on Equation 19, we can calculate the total work of an RVE subject to a static elasto-plastic deformation by integrating the work rate over time sequence and spatial domain  $\Omega_{0m}$  in the following equation where its second line is further derived by invoking the Hill-Mandel energy condition of Equation 1 and by assuming the rates of strains are within the hyperspace of the virtual strains:

$$W = \int_t \int_{\Omega} \hat{W} d\Omega_{0m} dt = \int_t \int_{\Omega} \mathbf{S}_m : \dot{\mathbf{E}}_m d\Omega_{0m} dt \quad (20a)$$

$$W = |\Omega_{0m}| \int_t \mathbf{S}_M : \dot{\mathbf{E}}_M dt = |\Omega_{0m}| \int_t \mathbf{S}_M d\mathbf{E}_M \quad (20b)$$

We can also write the total work  $W$  as a summation of total strain energy  $W^{el}$  and total plastic work  $W^{pl}$  as:

$$W = W^{el} + W^{pl} \quad (21)$$

where the total strain energy of the RVE can be further derived by assuming linear elasticity in the constitutive relation as:

$$W^{el} = \int_t \int_{\Omega} \mathbf{S}_m : \dot{\mathbf{E}}_m^{el} d\Omega_{0m} dt = \int_{\Omega} \int_{\mathbf{E}_m^{el}} \mathbf{S}_m d\mathbf{E}_m^{el} d\Omega_{0m} = \frac{1}{2} \int_{\Omega} \mathbf{E}_m^{el} : \mathbb{C}_m^{el} : \mathbf{E}_m^{el} d\Omega_{0m} \geq 0 \quad (22)$$

where  $\mathbb{C}_m^{el}$  represents the elastic modulus at a micro-point. It is equal to  $(1 - D_m)\mathbb{C}^{el}$  if damage occurs and  $\mathbb{C}^{el}$  if no damage happens. Considering the fact  $0 \leq D_m \leq 1$ , it is straight forward to see  $W^{el} \geq 0$ .

The total plastic work can be computed by integrating the rate of plastic work over time and spatial domains, and it is equal to the sum of total energy dissipation and total plastic free energy as:

$$W^{pl} = W^{di} + W^{pf} \quad (23)$$

On the one hand, the total energy dissipation can be expressed as the integration of non-negative dissipation rate, i.e.,  $\Phi \geq 0$  as:

$$W^{di} = \int_t \int_{\Omega} \Phi d\Omega_{0m} dt \geq 0 \quad (24)$$

On the other hand, we can compute the total plastic free energy as the integration of the rate of the plastic free energy as:

$$W^{pf} = \int_t \int_{\Omega} \dot{\psi}^{pl} d\Omega_{0m} dt = \int_{\Omega} \psi^{pl} d\Omega_{0m} \quad (25)$$

where  $\psi^{pl}$  stands for the density of the plastic free energy over the RVE domain, which can be further decomposed into isotropic and anisotropic parts [18] as:

$$\psi^{pl} = \psi_{iso}^{pl} + \psi_{ani}^{pl}; \quad \psi_{ani}^{pl} = \psi_{kin}^{pl} - \psi_{dis}^{pl} \quad (26)$$

where  $\psi_{iso}^{pl}$ ,  $\psi_{ani}^{pl}$ ,  $\psi_{kin}^{pl}$  and  $\psi_{dis}^{pl}$  represent the constituents of plastic free energy density from isotropic, anisotropic, kinematic and distortional mechanism. We note that the distortional constituent  $\psi_{dis}^{pl}$  is associated to the distortional strain hardening with directional distortion of yield surfaces, which is out of the scope of this work. For the isotropic and kinematic parts, we can write their expressions [19] as:

$$\psi_{iso}^{pl} = \frac{c_1}{2\rho} \bar{k}^2; \quad \psi_{kin}^{pl} = \frac{c_2}{2\rho} \bar{\alpha}_{ij} \bar{\alpha}_{ij} \quad (27)$$

where  $\bar{k}$  and  $\bar{\alpha}_{ij}$  are the thermodynamic conjugates to the size of the yield surface and deviatoric back stress tensor representing the center of the yield surface.  $\rho$  is the material density, while both  $c_1$  and  $c_2$  are two non-negative material constants depending on the type of material models. The total plastic free energy can be therefore expressed as:

$$W^{pf} = \int_{\Omega} \left( \frac{c_1}{2\rho} \bar{k}^2 + \frac{c_2}{2\rho} \bar{\alpha}_{ij} \bar{\alpha}_{ij} \right) d\Omega_{0m} \geq 0 \quad (28)$$

By plugging Equations 22, 24 and 28 into Equation 20b, we are ready to show that for an arbitrary macroscale material point associated with an RVE, as it is subject to general plastic hardening and softening deformations, its effective macroscale stress and strain fields satisfy the constraint in Equation 29. We incorporate this constraint together with the non-decreasing damage variable described in Section 2.2 as physics information into the data-driven model in the next section.

$$\int_t \mathbf{S}_M d\mathbf{E}_M \geq 0 \quad (29)$$

### 3 Physics-informed data-driven surrogate

In this section, we propose a computational framework of physics-constrained data-driven model to emulate the lower level homogenization procedures in multiscale simulations. Our framework starts with the database generation in Section 3.1. The database contains a set of systematically sampled microstructural deformation-response sequences which the data-driven surrogate in Section 3.2 is trained on. To improve the model’s efficacy, we incorporate two physics constraints by creating a novel RNN architecture and demonstrate its superior performance in Section 3.3. In Section 3.4, we show the integration procedure of our surrogate within multiscale solvers.

#### 3.1 Database generation

The first step of developing a data-driven surrogate is to generate a database that emulates underlying functional space via sufficient sampling. Comparing to the sampling on non-sequential variables, the dimension of the sampling space of temporal variables is much larger, as it requires a sequence of time-related data rather than a single data for each sample feature. To better exploit the sampling space of temporally varying deformation paths, we use DoE to systematically create a set of random strain paths.

In the DoE, we assume every strain path starts from relaxing state with zero initial strain without residual stress, and it evolves to final state by a number of loading steps. To reduce the dimension of deformation space, we assume the strain values at any step should be no larger than a user-defined threshold  $\zeta_1$ . In addition, we assume the bulk modulus of our material is fairly large such that the deformation-induced volume change is within a user-defined limit  $\zeta_2$ . Accordingly, we can express the two sampling constraints as:

$$|E_n^i| \leq \zeta_1; \quad |E_n^{vol}| \leq \zeta_2 \quad (30)$$

where  $E_n^i$  represents the  $i^{th}$  component of the strain vector at the time step  $n$  where  $i \in \{1, 2, 3, 4, 5, 6\}$  indicates the six components of 3D strains.  $E_n^{vol} = \Delta|\Omega_{0m}|/|\Omega_{0m}| = E_n^1 + E_n^2 + E_n^3$  stands for the volumetric strain that accounts for the RVE’s volume change  $\Delta|\Omega_{0m}|$  after deformation. Considering our material’s property (see Section 4 for details), we set the two DoE constraints as  $\zeta_1 = 10\%$  and  $\zeta_2 = 4\%$  in our work.

For the generation of random loading sequences, we set all deformation paths to have the same number of loading steps  $n_{load}$ . More precisely, we select  $n_c$  evenly spaced control points among loading steps, and assign them with strain values drawn from random processes, e.g., Sobol sequence or Latin hypercube sampling. Without loss of generality, we assume  $n_{load} = 100$  and  $n_c = 5$ . In order to enforce all strain components at the control points to satisfy the DoE constraint in Equation 30, we first generate random values for shear strain components satisfying  $|E_c^{\{3,4,5\}}| \leq 10\%$ . Then, to fulfill the constraint of volume change, we sample the random values for two out of the three normal strain components and volumetric strain, and let them subject to the constraints  $|E_c^{\{1,2\}}| \leq 10\%$  and  $|E_c^{vol}| \leq 4\%$ . The value of the third normal strain component is therefore equal to  $E_c^{vol} - E_c^1 - E_c^2$ .

With random strain values generated at  $n_c$  control points, we proceed to use Gaussian process (GP) to interpolate the strain values at all  $n_{load}$  loading steps. The reason we choose GP over other interpolators is to create continuous and smooth sampling strain paths as in the mechanistic simulations. By considering the strain components as random variables, GP

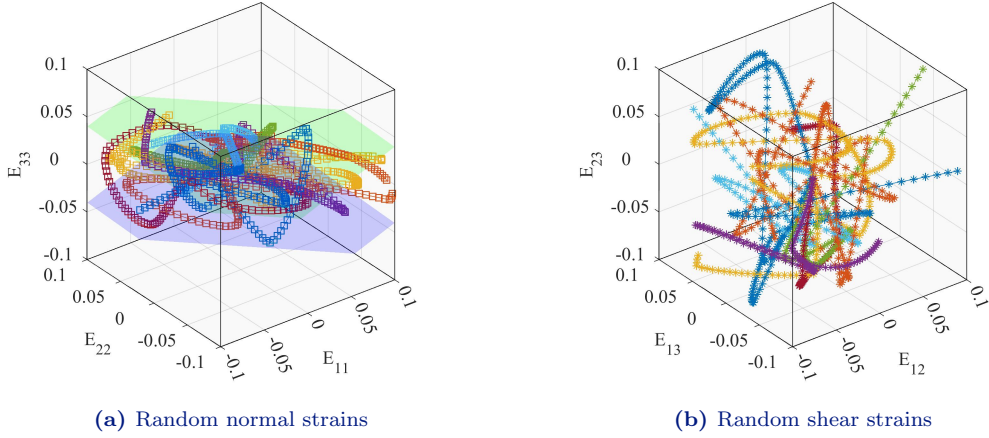


**Figure 2 Illustration of random deformation paths:** We demonstrate ten random sampling strain paths generated by GP in the DoE process with the normal strain components in (a) and shear strain components in (b).

models random strain values following multivariate Gaussian distributions. Specifically, we can emulate each of the six strain components per sampling sequence via a one-dimensional GP with a mean function  $m(z)$  and a covariance function  $c(z, z')$  as:

$$E^i(z) \sim GP(m(z), c(z, z')) \quad (31)$$

where the GP input parameters  $z$  and  $z'$  represent two different time instances or loading steps in a loading sequence, and  $E^i(z)$  is the  $i^{th}$  component of the strain at the time instance  $z$ . For the interpolation, we adopt a simple GP model with a zero mean and a covariance function with a Gaussian kernel  $r$  as:

$$c(z, z') = \sigma^2 r(z, z'); \quad r(z, z') = \exp(-w(z - z')^2) \quad (32)$$

where the covariance function  $c$  depends only on the prior variance  $\alpha^2$ , the roughness parameter  $w$ , and the distance between input parameters  $z$  and  $z'$ . To generate random samples at steps  $n_{load}$  from the control points at  $n_c$ , we create random strain sequences by using the one-dimensional GP in Equation 31 to individually interpolate each strain component.

We create a total of 30,000 deformation paths through the GP, and each path accounts for the temporal evolution of six independent strain components. Ten out of the 30,000 strain paths are plotted in Figure 2 for illustration. It is evident from the figure that while the random shear strains tend to span the entire hypercube-like sampling space defined by the constraint  $\zeta_1$ , the sequences of normal components are additionally confined between the two hyper-planes representing the volumetric strain constraint  $\zeta_2$ .

After we generate random macroscale strain paths from DoE, we proceed to compute their corresponding effective RVE responses. To compute microstructural effective responses, we apply all the 30,000 strain sequences in the computational homogenization. More precisely, we apply the random macroscopic strain sequences to impose microstructural displacement boundary conditions using affine boundary condition as:

$$\mathbf{u}_m(\mathbf{p}) = \mathbf{E}_M \Delta \mathbf{p} \quad \forall \mathbf{p} \in \Gamma_{0m} \quad (33)$$

where the displacement boundary condition  $\mathbf{u}_m$  is based on the macro-strain tensors  $\mathbf{E}_M$  and the relative coordinates  $\Delta\mathbf{p}$  of the nodes on the microstructural boundary  $\Gamma_{0m}$ . We then solve the microstructural local stress  $\mathbf{S}_m$  from the BVP, and compute the effective stress from Equation 2 and the effective damage parameters [14] by:

$$D_M = 1 - \frac{\|\mathbf{S}_M : \mathbf{S}_M^0\|}{\|\mathbf{S}_M^0 : \mathbf{S}_M^0\|} \quad (34)$$

where the homogenized damage parameter  $D_M$  indicates the damage status of the RVE, depending on the values of the effective stress  $\mathbf{S}_M$  and the reference stress  $\mathbf{S}_M^0$  in the absence of damage from Equation 5.

We solve all the microscopic BVP on a simple RVE with its geometry and mesh illustrated in Figure 3. In our RVE, a spherical pore at the center is surrounded by the material matrix with its property detailed in Section 4. To perform microscale BVPs, our first choice is to perform FEM by discretizing the RVE’s domain with 15,000 tetrahedral elements as shown in Figure 3(b).

Even though classic finite element method (FEM) can provide high-fidelity solutions to our BVPs, its simulation process is typically time consuming. The total computational cost of FEM to generate the response database for the 30,000 deformation paths is therefore prohibitively expensive. In order to efficiently generate the database, we apply our previously developed mechanistic-based ROM [5] to perform the simulations. Compared to FEM, our ROM strikes a good balance between efficiency and accuracy by agglomerating elements into clusters. An example of the ROM’s clustering is demonstrated in Figure 3(c). We emphasize that a mesh independence study is required in softening simulations to ensure solution convergence and sequentially, choose a proper discretization level, as discussed in Section 2.2. Our investigation of microscale mesh convergence in Appendix A shows that our ROM with 1,200 clusters results in consistent post-failure responses as the high-fidelity FEM solutions but only uses less than 10% of computational time. Therefore, we adopt our mechanistic-based ROM to replace FEM for the database generation and considers ROM as the benchmark when comparing to data-driven surrogates in the following sections. To the end, our entire database is created by ROM with 30,000 deformation-response sequences, and each sequence contains 100 loading steps. At each loading step, it contains six macro-strain components, and seven effective RVE responses including six stress components and one damage parameter.

## 3.2 Data-driven surrogate

After we generate the training database in Section 3.1, we present pure data-driven neural networks and RNN in the Subsections 3.2.1 and 3.2.2, respectively, and we discuss the limitations of classic RNN in processing long sequential data.

### 3.2.1 Feed forward neural networks

Artificial Neural Network (ANN) is well recognized for its representational capability. The most basic type of ANN is the multi-layer perceptron, also known as the feed-forward neural network (FFNN), which is a collection of neurons arranged in multiple layers such that each neuron has one-way connections to the neurons of the subsequent layer. If a FFNN is fully connected, every neuron is connected to all neurons of the subsequent layer.

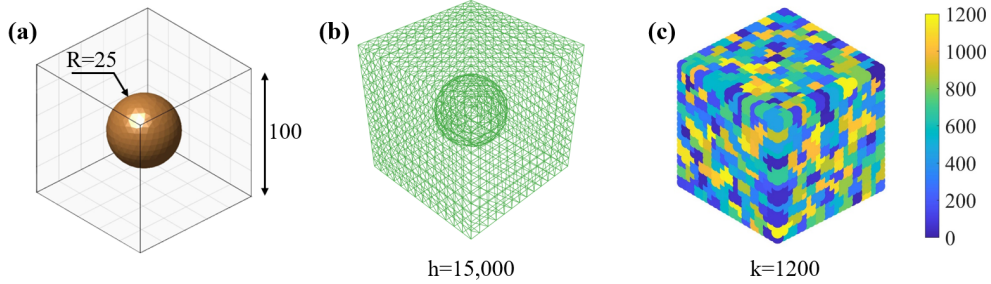


**Figure 3 The geometry and mesh of our RVE:** (a) The dimension (unit:  $\mu m$ ) of our RVE that contains a spherical pore at center with a pore volume fraction of 6.25%; (b) The finite element discretization with 15,000 elements; and (c) RVE’s ROM with 1,200 clusters.

A simple fully-connected FFNN with two input neurons, one hidden layer with three neurons, and a single-neuron output layer is shown in Figure 4 in which each neuron performs a mathematical operation that adds a bias to the weighted sum of its inputs, followed by an activation function [20]. While different types of activation functions can be chosen based on learning tasks at hand, common choices include hyperbolic tangent, rectified linear unit (ReLU), leaky ReLU, and swish. Mathematically, the neuron in Figure 4(b) transforms inputs into outputs by a composition of weighted summation and activation functions as:

$$\mathbf{x}^{(l-1)} = f(\mathbf{W}^{(l)}\mathbf{x}^{(l-1)} + \mathbf{b}^{(l)}) \quad (35)$$

where  $f$  is the nonlinear activation function of choice, and  $\mathbf{x}^{(l-1)}$  and  $\mathbf{x}^{(l)}$  represent the inputs from the lower layer  $l - 1$  and the outputs at the current layer  $l$ , respectively. Additionally,  $\mathbf{W}^{(l)}$  and  $\mathbf{b}^{(l)}$  are respectively the weight matrix and the bias vector on the current layer  $l$ . We note that both weights and biases are known as the network parameters as they are learned in the training process.

Based on the universal approximation theorem [20], which states that a multi-layer perceptron with a single hidden layer and a finite number of neurons can arbitrarily approximate any continuous function, various architectures and extensions have been proposed to explore the potential of FFNN to learn the underlying function of data-driven systems and constitutive models [21–23].

### 3.2.2 Recurrent neural network

Recurrent neural network (RNN), as a derivation from FFNN, was initially developed for ordinal or temporal problems to learn from sequential data [24]. There are several major differences between RNN and FFNN. First, the data order of an input sequence matters for RNN such that its output is dependent on both previous and current input values. Second, while FFNN learns training parameters separately for each neuron, RNN shares parameters within each layer of the network, leading to fewer trainable parameters and thus, higher training efficiency. Third, RNN’s parameters are typically learned through the algorithms of gradient descent and back propagation through time (BPTT). The BPTT varies from the regular back propagation as it computes the sum of errors at each time step.

To understand the working mechanism of RNN, let’s look at its computational graph in Figure 5(a) where a layer of RNN cells relate the input sequence  $\mathbf{x}_t$  to a series of outputs  $\mathbf{y}_t$  with  $t$  representing an pseudo-time instance within a total of  $q$  time steps. Specifically,

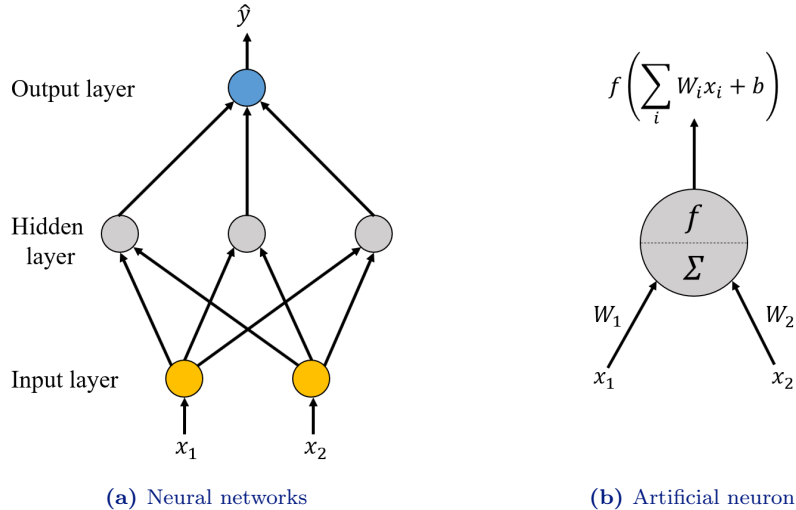


**Figure 4 Illustration of neural networks:** (a) A shallow FFNN with two input neurons, one hidden layer with three hidden neurons, and single output neuron; and (b) Illustration of the mathematical operations in a hidden neuron.

as time propagates, the network unfolds itself such that the temporal-dependent RNN cells sequentially connect one to another to pass down memory-like hidden variables. The mathematical operations in the RNN cell at time step  $t$  in Figure 5(b) can be expressed as:

$$\mathbf{h}_t = \tanh(\mathbf{W}_{hh}\mathbf{h}_{t-1} + \mathbf{W}_{xh}\mathbf{x}_t + \mathbf{b}_h) \quad (36a)$$

$$\hat{\mathbf{y}}_t = \mathbf{W}_{hy}\mathbf{h}_t + \mathbf{b}_y \quad (36b)$$

where hyperbolic tangent is chosen as the activation function, and the hidden state  $\mathbf{h}_t$  at the current step is computed from the current input state  $\mathbf{x}_t$  and the previous hidden state  $\mathbf{h}_{t-1}$ . In addition,  $\mathbf{W}_{xh}$ ,  $\mathbf{W}_{hh}$ , and  $\mathbf{W}_{hy}$  are weighting matrices corresponding to input-to-hidden, hidden-to-hidden, and hidden-to-output affine transformations, respectively.  $\mathbf{b}_h$  and  $\mathbf{b}_y$  are the bias terms for the current hidden variables and output estimations.

The major issues that RNN suffers from when processing long sequential data are the vanishing and exploding gradients [25]. While vanishing gradient occurs when the magnitude of gradients continuously decreases as the learned weights eventually become insignificant, the exploding gradient results in extremely large updates to weights during training, and causes unstable learning process. These issues lead to the further development of more advanced sequence learners, e.g., long short-term memory (LSTM) [26] and gated recurrent unit (GRU) [27]. We adopt GRU in our RNN model due to its high efficiency and we review its working mechanism in Appendix B.

### 3.3 Incorporation of physics constraints within RNN

Pure data-driven RNN often requires a large amount of sequential data for training. Considering the high computational costs of 3D elasto-plastic simulations for the data generation of deformation-response sequences, it is more feasible for us to reduce number of the sampling data sequences and create a moderate size of training dataset upon which a physics-constrained RNN can outperform pure data-driven counterparts. To this end, we explore

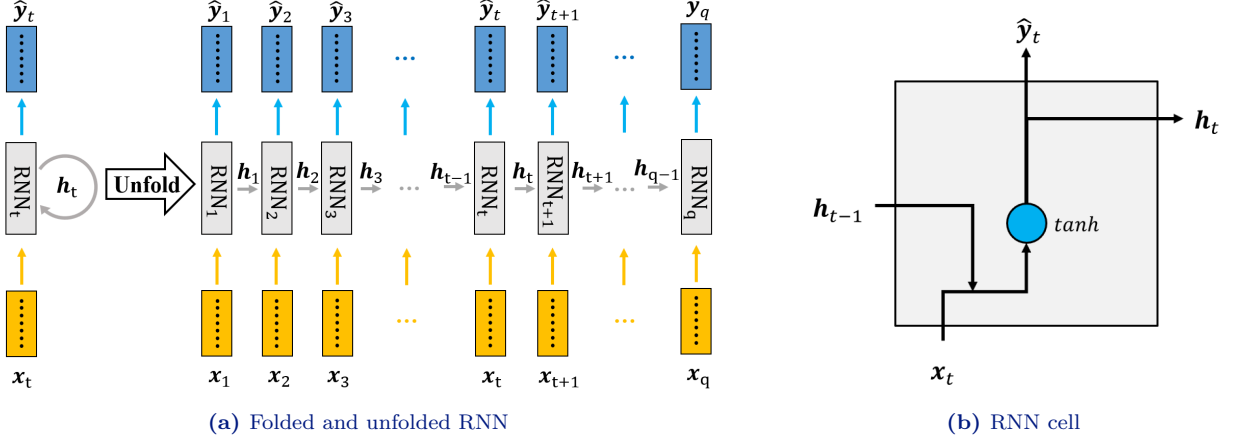


**Figure 5 Computational graph of RNN:** (a) Folded and unfolded representations of RNN’s architecture that maps a sequence of inputs to a sequence of outputs with hidden state variables passing down cells as system memory where  $t$  represents an pseudo-time instance in a total of  $q$  time step; and (b) Demonstration of the internal structure and data flow of one RNN cell at the time instance  $t$  where a hyperbolic tangent function maps the weighted current inputs and prior hidden variables to the current outputs and hidden variables.

two types of physics constraints in Section 3.3.1, and incorporate them into our data-driven model by customizing model architectures. We proceed to demonstrate the improved performance of our RNN by comparing to a vanilla (pure data-driven) model in Section 3.3.2.

### 3.3.1 Physics constraints

In training process, a loss function is iteratively minimized to update learning parameters through BPTT, and for RNN models, a generic loss function  $l_t^0$  of the RNN cell at an arbitrary time instance  $t \in \{1, 2, \dots, q\}$  can be defined as:

$$l_t^0 = \frac{1}{d_{out}} \frac{1}{n_b} \sum_{b=1}^{n_b} \|\mathbf{y}_t^b - \hat{\mathbf{y}}_t^b\|_{L1}^2 \quad (37)$$

where  $\mathbf{y}_t$  and  $\hat{\mathbf{y}}_t$  represent the ground truth and predicted values of the outputs including six homogenized stress components  $\mathbf{S}_t$  and one effective damage parameter  $D_t$  at the time instance  $t$ , i.e.,  $\mathbf{y}_t = (\mathbf{S}_t, D_t)$ .  $d_{out}$  is the dimension of outputs, and  $\|\cdot\|_{L1}$  indicates the  $L1$  norm of vectors. In addition,  $b$  represents the index in a training batch of size  $n_b$ .

As we have shown in Equation 29 of Section 2.4 that the total internal work at an arbitrary macro-point can be computed from its associated RVE’s homogenized stress and strain, and the work value is always non-negative. We can therefore incorporate this constraint into the generic loss function by using a penalty term as:

$$l_t = l_t^0 + \lambda l_t^1; \quad l_t^1 = \frac{1}{n_b} \sum_{b=1}^{n_b} ReLU\left(-\sum_t (\hat{\mathbf{S}}_t^b : \Delta \mathbf{E}_t^b)\right) \quad (38)$$

where  $l_t$  is the total loss function for the RNN cell at the time instance  $t$ , and  $l_t^1$  is the augmented penalty term associated with the internal work in Equation 29. We approximate the total internal work by the sum of incremental internal work, which is computed by the predicted current stress  $\hat{\mathbf{S}}_t^b$  and the incremental strain  $\Delta \mathbf{E}_t^b$  in a training batch, i.e.,  $\Delta \mathbf{E}_t^b =$



$\mathbf{E}_t^b - \mathbf{E}_{t-1}^b$ . To penalize any violation of the work constraint, We adopt a non-negative penalty parameter, i.e.,  $\lambda \geq 0$ , and a rectified linear unit (ReLU), i.e.,  $ReLU(x) = \max(x, 0) \geq 0$ , such that a negative internal work would increase the total loss value during minimization, and thus result in penalty on such constraint violation. We note that the value of the penalty parameter  $\lambda$  is case-dependent and often carefully chosen to balance the weights of the generic loss and the penalty term as it affects learning efficiency and could pose challenges to the overall training process. In this work we empirically set its value as  $10^{-6}$ .

Our second constraint is based on the fact that our material is not self-healing in the irreversible damage process such that the damage parameter  $D_t$  at an arbitrary macro-point is non-decreasing as damage proceeds:

$$\frac{\partial D_t}{\partial t} \geq 0 \quad (39)$$

where  $D_t$  is the effective macro damage parameter at time  $t$  that can be computed from the RVEs' homogenized damaged and reference stresses in Equation 34. However, the condition of non-decreasing damage parameter is not necessarily satisfied by the vanilla architecture in Figure 5(a) and thus, we have to develop a numerical scheme to explicitly enforce the irreversible damage process.

To incorporate such damage constraint, we propose a new RNN architecture by introducing several major modifications of the vanilla model as shown in Figure 6. Specifically, we firstly attach two FFNNs to the outputs of RNN (using GRU cells), and assume the FFNNs' outputs are the effective reference stress in the absence of damage and the damage parameter  $\hat{D}_t$  at the time instance  $t$ . The underlying reason for us to choose the reference stress instead of damaged stress as the FFNNs' outputs is that we tend to let our RNN to learn the stress based on a much simpler elasto-plastic hardening relation given our moderate size of training dataset. On the contrary, if we select damaged stress as outputs, as the softening simulation involves much more complex behaviors, a representative RNN model would require more learning parameters that needs to be trained on a larger dataset. To enforce the damage irreversibility, We compute the damage increment by comparing its predictions at the current step  $\hat{D}_t$  and previous step  $\hat{D}_{t-1}$  and accordingly update the damage parameter by using the following scheme:

$$\hat{D}'_t = \sum_t \{\hat{D}_t + \Delta \hat{D}_t [\text{sgn}(\Delta \hat{D}_t) \times 0.5 - 0.5]\}; \quad \Delta \hat{D}_t = \hat{D}_t - \hat{D}_{t-1} \quad (40)$$

where  $\hat{D}'_t$  indicates the corrected output of the effective damage parameter at the time instance  $t$ , and  $\Delta \hat{D}_t$  represents the incremental difference between two consecutive steps. We proceed to apply the sign function  $\text{sgn}(\cdot)$  to  $\Delta \hat{D}_t$  to mark the time instance at which damage estimation decreases compared to their previous value. We then use the sign function to compensate the FFNNs-estimated damage parameter  $\hat{D}_t$  by the incremental errors accumulated from the initial time instance. We then apply a normalization function to ensure  $\hat{D}'_t$  to stay within the bounds of  $[0, 1]$ .

With the corrected damage parameter  $\hat{D}'_t$  and FFNNs-estimated reference stress  $\hat{\mathbf{S}}_t^0$ , we can now compute the damaged stress by following the same relation as the continuum damage

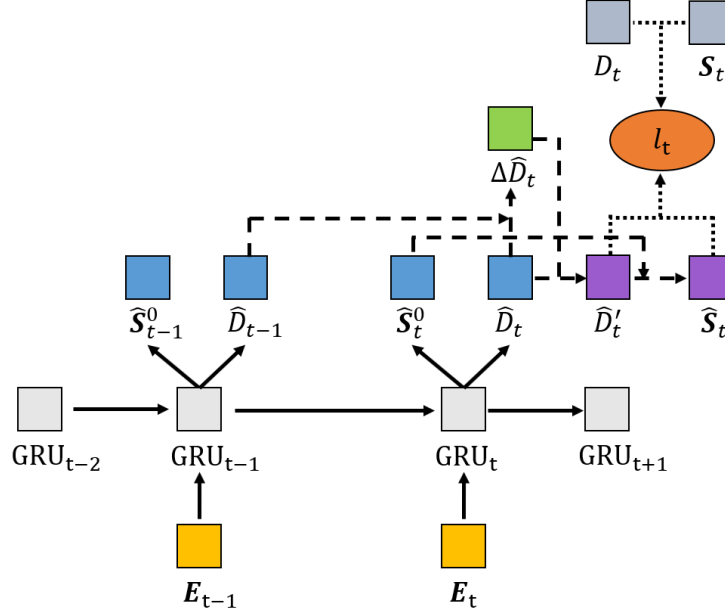


**Figure 6 Computational graph of the proposed RNN architecture:** Demonstration of the inputs, outputs, intermediate variables, and the loss function for the data flow of the cell at the time step  $t$  where we adopt GRU cell within our RNN architecture.

mechanics in Equation 5 as:

$$\hat{\mathbf{S}}_t = (1 - \hat{D}'_t) \hat{\mathbf{S}}_t^0 \quad (41)$$

where  $\hat{\mathbf{S}}_t$  corresponds to the corrected stress components. Comparing the corrected damage and stress values to their ground truths, we are able to compute the loss function at the time instance  $t$  from Equation 38.

We emphasize that we enforce the two physics constraints within our RNN by using two different approaches. While we implement the energy constraint in Equation 38 as a soft constraint by adding an associated penalty term in the loss function, we enforce the damage constraint in Equation 39 as a hard constraint by imposing architectural modifications and output post-processing using network parameters. Upon comparing the two approaches, We note that although the hard constraint always guarantees constraint's enforcement, it may lead to a stiffer optimization problem [28] during training. Additionally, its architectural modifications involve significant model development efforts, and such modifications may become infeasible for more complex problems. Therefore, the choice of a hard or soft approach is situational, and it needs more investigations in future study.

### 3.3.2 Impacts of constraints

To demonstrate the impacts of the two physics constraints, we compare the prediction accuracy by comparing a vanilla model against our RNN model. For this comparison, we randomly choose 200 samples out of the total 30,000 RVE deformation-response sequences as a test set, and train the two models on the five databases of different sizes including 6,000, 12,000, 18,000, 24,000 and 29,800. In all databases, We split the data into 80% for training set and 20% for validation set. While the training set is utilized in optimization to iteratively update learning parameters, the validation set is used to monitor the overall training procedure to avoid overfitting or underfitting.

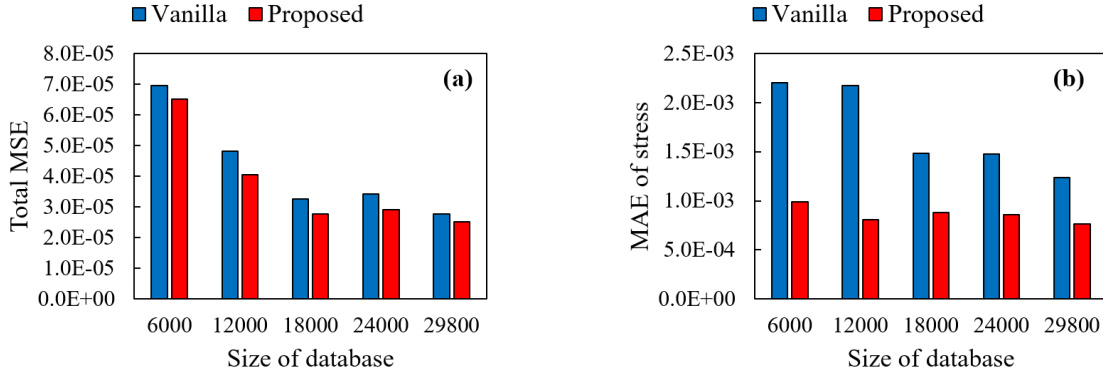


**Figure 7 Comparison of training errors:** (a) Comparison of total MSE between the vanilla model and our proposed RNN architecture on different sizes of training datasets; and (b) Comparison of MAE on the predicted effective stress with respect to the sizes of training datasets.

In training, we start with normalizing all data sequences to the range of  $[0, 1]$ . By setting the training epochs as 1,200 with a batch size of 64, we choose *Adam* as the optimizer in both models with an adaptive learning rate that starts at  $10^{-3}$  and reduces by 25% when the validation error is not reduced over 30 training epochs. Our training process is terminated when training reaches the 1,200 epochs or the loss function is not improved by  $10^{-7}$  in 50 epochs. Our loss function is defined by the mean squared error (MSE), and the validation metric is chosen as the mean absolute error (MAE). After training, We compare the two models’ prediction errors on the same 200 samples in the test set that is unseen from the entire training process as in Figure 7.

We have several observations from Figure 7. For the overall MSE in Figure 7(a), we find as the sizes of databases increase from 6,000 to 29,800, both models’ MSE decreases dramatically from about  $7 \times 10^{-5}$  to  $3 \times 10^{-5}$ . In all cases, the MSE of our proposed model is clearly lower than the vanilla counterpart. In terms of the predictions on the damaged stress in Figure 7(b), the proposed model evidently demonstrates a superior accuracy than the vanilla model. Specifically, on the smaller databases (6,000 or 12,000) when we are only accessible to a limited amount of training data, the MAE of our model is less than 40% of the baseline model clearly demonstrating the importance of physics constraints in regularizing data-driven models. On the contrary, as the sizes of databases increase, we observe the MAE gap narrows between the two models, as the pure data-driven vanilla model is shown more sensitive to the amount of data.

### 3.4 Data-driven multiscale analysis

In our data-driven multiscale simulations, we use the trained RNN as a surrogate to replace the expensive micro-analysis solver, e.g., FEM or ROM. However, the online deployment of RNN emulator within a physical solver is more difficult than its training process. This is because, during training, RNN is accessible to the convergent deformation and effective response histories at all  $n_{load}$  loading steps. Comparatively, in online computations, the trained RNN can only access to convergent strain and response histories from previous steps, as it lacks the convergence information at both the current step and future steps. We address this issue by explicitly modifying the data structure of RNN input sequences and implicitly resetting RNN’s hidden variables amid iterations.

We demonstrate the approach to incorporate our trained RNN into a multiscale model by the pseudo-code in Algorithm 1. In nonlinear material simulations, Newton Raphson method is a classic numerical approach to iteratively solve for material responses. This method essentially consists of a double-loop structure: while the outer loop accounts for the steps with different loading conditions, the inner loop iterates material responses under a certain loading condition until convergence, i.e., equilibrium between internal and external forces.

In a typical step of a multiscale simulation, we compute the macro strain at an arbitrary material point from equilibrium equations within the inner loop. By appending the strain at the current iteration to the sequence of previous convergent strains, we find the sequence’s length is only equal to the current load step number and smaller than the RNN input sequence length  $n_{load}$ . We then add replicate padding by repeating the current strain multiple times to the end of the strain sequence. It not only makes the strain sequence compatible with RNN inputs, but also implicitly enforcing the RNN’s hidden variables at the current step to stay constant within iteration loops, as the current hidden variables dependent on pre-trained network parameters and the inputs at early time instances, see Equation 36. The underlying reason of using the same values of hidden variables at the current step is similar to the classic radial return algorithm in plastic analysis where material state variables are only updated upon convergence. We also emphasize that the loading step number of the multiscale model should be smaller than or equal to the sequence length of RNN inputs  $n_{load}$ , as a larger step number would result in data truncation and erroneous RNN inference.

---

**Algorithm 1:** Integration of RNN in multiscale analysis

---

```

i = 1, 2, . . . , nload ;                               /* Newton step number */
j = 1, 2, . . . , niter ;                               /* Newton iteration number */
while i ≤ nload do
  while j ≤ niter do
    (1) Read macro strain  $\mathbf{E}_i^j$  from macro equilibrium equation
    (2) Append  $\mathbf{E}_i^j$  to the convergent strain sequence  $\{\mathbf{E}_1^c, \mathbf{E}_2^c, \dots, \mathbf{E}_{i-1}^c, \mathbf{E}_i^j\}$ 
    (3) Add (nload - i) replicate padding of  $\mathbf{E}_i^j$  to the end of the sequence in (2)
    (4) Perform RNN inference on the updated strain sequence
    (5) Read RNN’s outputs for the effective responses at the step i
    (6) Solve macro equilibrium equation
     $\epsilon = 10^{-6}$  ;                                     /* convergence criterion */
    if  $\|\mathbf{f}_{int} - \mathbf{f}_{ext}\| \leq \epsilon$  then
      | Update convergent strain  $\mathbf{E}_i^c = \mathbf{E}_i^j$ 
      | Proceed to the next loading step: i ← i + 1
    else
      | Proceed to the next iteration: j ← j + 1
    end
  end
end
end

```

---

## 4 Numerical experiments

We demonstrate the efficiency and accuracy of the proposed physics-constrained data-driven surrogate on the multiscale damage simulations in this section. We assume the material as aluminum alloy A356 with elastic modulus of  $5.7e4$  MPa and the Poisson’s ratio of 0.33. Its elasto-plastic hardening behavior is assumed as isotropic and follows associated plastic flow rule with the Mises yield surface defined by:

$$S \leq S_y(\bar{E}^{pl}) \quad (42)$$

where  $S$  and  $S_y$  are respectively the Mises equivalent stress and yield stress depending on the equivalent plastic strain  $\bar{E}^{pl}$ . To model strain hardening, we assume the relation between  $S_y$  and  $\bar{E}^{pl}$  as piecewise-linear as shown by the hardening curve in Figure 8. For softening simulations, we employ the damage continuum model as discussed in Section 2.2 with the fracture strain  $E_f$  of 0.067 and the fracture energy  $G_f$  of  $1.92e4$  N/m.

This section is organized as follows: we first illustrate the efficacy of our physics-informed RNN in predicting microstructural effective stress and damage solutions in Section 4.1 where we assume micro-porosity as the only material defects in our work. We proceed to demonstrate the simulation of multiscale elasto-plastic hardening and softening behaviors in Section 4.2 by integrating micro-RNN with macro-FE solver. In Section 4.3, we perform a mesh convergence study on a macro-component with varying discretization levels to validate damage patterns. In all experiments, We record computational costs and provide accuracy analysis for the insight of our method’s performance.

We implement the RNN models in Python using the deep learning packages: TensorFlow and Keras. For the development of RNN models, the database of microstructural effective behaviors is generated on a state-of-the-art high-performance cluster (HPC) with 60 CPU cores (AMD EPYC processors) and 360 GB RAM. The RNN models are trained on the same HPC using two GPU units (NVIDIA Tesla v100) with 32 GB RAM. To pipeline multiscale simulations, we develop a dedicated program to integrate the RNN models as the microstructural solver with our multiscale engine which is implemented in Matlab. All data-driven multiscale computations in Sections 4.2 and 4.3 are conducted on a 64-bit Windows desktop with four CPU cores (Intel i7-3770) with 16 GB RAM.

### 4.1 Microstructural simulations via RNN

In order to use RNN to replace microstructural analyses, we need to assert its prediction accuracy under various loading paths. As discussed in Section 3.1, to cover as much as the deformation space, we generate a database containing 30,000 strain paths by DoE where each path contains six strain components at 100 sequential loading steps. To efficiently generate the database, we use ROMs to simulate the microstructural effective softening behaviors, see Section 3.1. Generation of the database takes about 10 days by exploiting parallel computing with 60 CPU cores on the HPC.

For RNN training, we exclude 200 deformation paths from the database for the testset and divide the other 29,800 paths into training set (80%) and validation set (20%). Our RNN model is then trained with 2000 epochs and a batch size of 64 by two GPU processors. After 4.3 hours’ training, our model reaches a final learning rate of  $7.53 \times 10^{-7}$  and a MSE

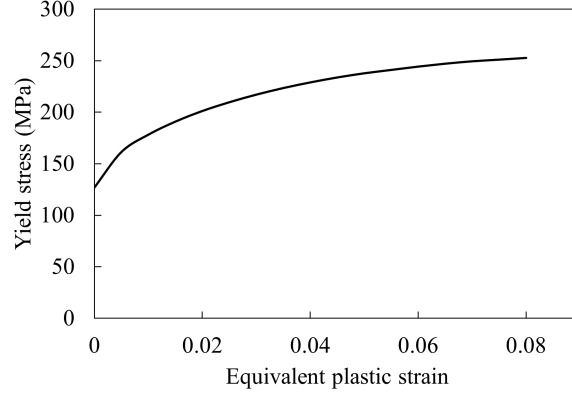


**Figure 8 Material’s hardening behavior:** we use a piecewise linear hardening model to define the elasto-plastic behavior of aluminum alloy A356.

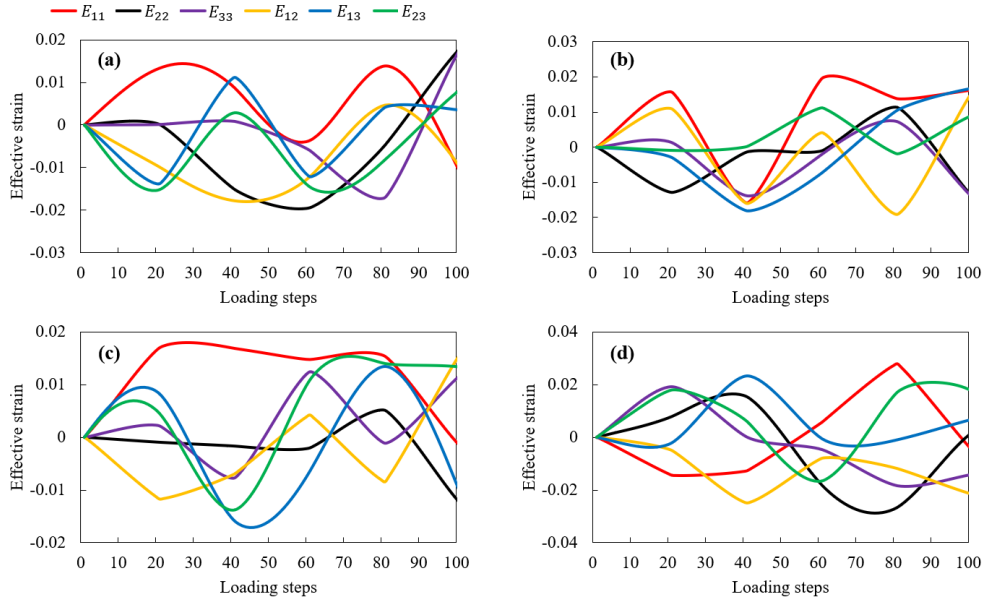


**Figure 9 Samples of strain paths:** Four samples of strain paths are randomly selected from the testset where each path contains six strain components with 100 sequential loading steps.

value of  $3.29 \times 10^{-6}$  on the training set. To demonstrate its accuracy, we randomly select four strain paths from the testset which are unseen from the entire training process in Figure 9, and compare the RNN predictions with the ground truth in Figure 10.

It is evident from Figure 10 that for different strain paths, the trained RNN is able to provide close estimations on the effective stresses and damage variables to the ground truth where the MSE on the testset is as small as  $6.69 \times 10^{-6}$ . We also observe that as the damage variable gradually increases to 1.0, the effective stress values are significantly reduced, indicating a dramatic loss in the RVE’s load-carrying capacity.

## 4.2 Multiscale models accelerated by RNN

We have demonstrated our RNN can accurately predict microstructural effective responses under various deformation paths. We can now use the RNN as a faithful surrogate to the computationally expensive microstructural analysis in multiscale simulations.

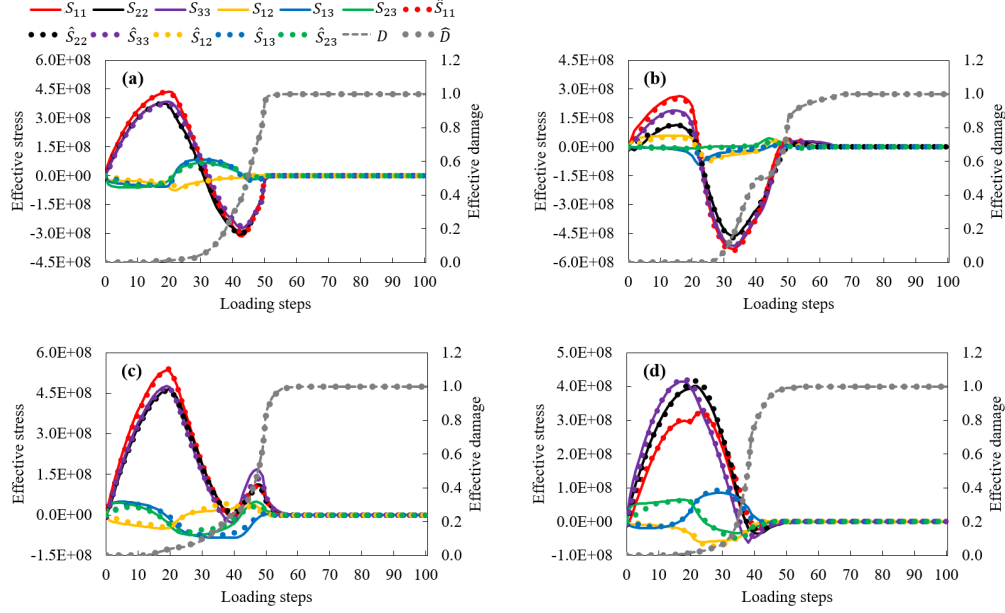


**Figure 10 Validation of microstructural effective responses:** Comparison between RNN predictions and ground truth of RVE effective stress components and damage variables for the four sampling strain paths in Figure 9 (a)-(d).

Our first multiscale simulation is performed on a 3D L-shape bracket as shown in Figure 11(a). The bracket is subject to a Dirichlet boundary condition on the left side while its right rim is fully constrained. We assume the bracket contains a multiscale domain at the sharp corner where we expect strain concentrations would occur. Specifically, each IP of the multiscale domain is associated with a porous RVE of Figure 3. To save computational costs, we assume outside the multiscale domain is a mono-scale domain where IPs are not associated with RVE. The bracket is meshed by 5300 tetrahedral elements of reduced integration, while the multiscale domain contains 360 elements which are associated with the RVE decomposed by 1200 clusters.

We first demonstrate the accuracy of the multiscale model for elasto-plastic hardening behaviors under complex cyclic loading path. To this end, we let the bracket subject to a loading-unloading-reloading scenario by setting the Dirichlet boundary condition as  $d = 0 \rightarrow 2 \rightarrow 0 \rightarrow -2$  mm. The resulting reaction force and displacement curves are compared by the proposed FE-RNN approach with the benchmark FE-ROM method in 11(b) where it is evident that the data-driven approach provides a high fidelity prediction in the reaction forces. We also compare the Von-Mises stress distributions by the two methods at  $d = -2$  mm in the Figure 12. We observe a generally good agreement between the two methods despite minor local discrepancy at the sharp corner as highlighted in the figure. A plausible reason for such discrepancy is that RNN's prediction power decreases at extreme values with insufficient training data points.

Our second multiscale experiment is to simulate the elasto-plastic hardening and softening on the same L-shape bracket where its Dirichlet boundary condition is set as  $d = 10$  mm. To prevent the occurrence of the non-physical single-layer fracture bands as discussed in Section 2.2, we apply a non-local damage function (see Equation 7) with the strain localization

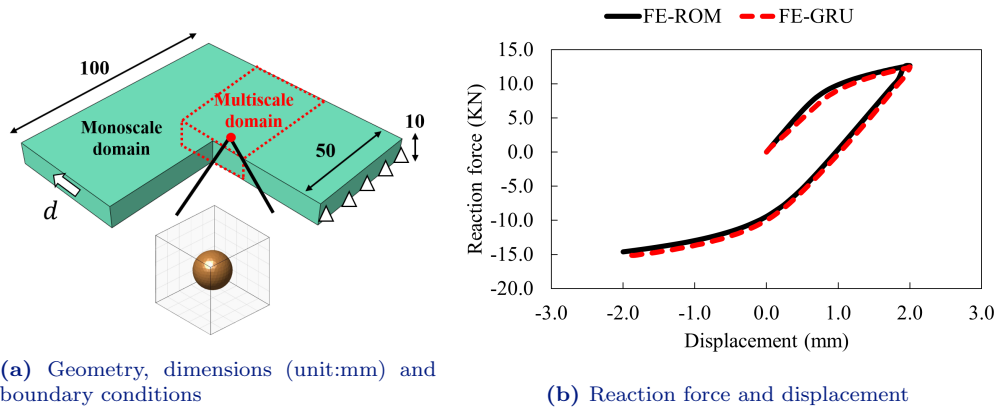


**Figure 11 Multiscale model of the L-shape bracket:** (a) Every macroscale integration point in the multiscale domain is associated with a microscale porous RVE; and (b) Comparison of the load-displacement curves of elasto-plastic hardening behaviors between FE-ROM and the proposed FE-RNN.

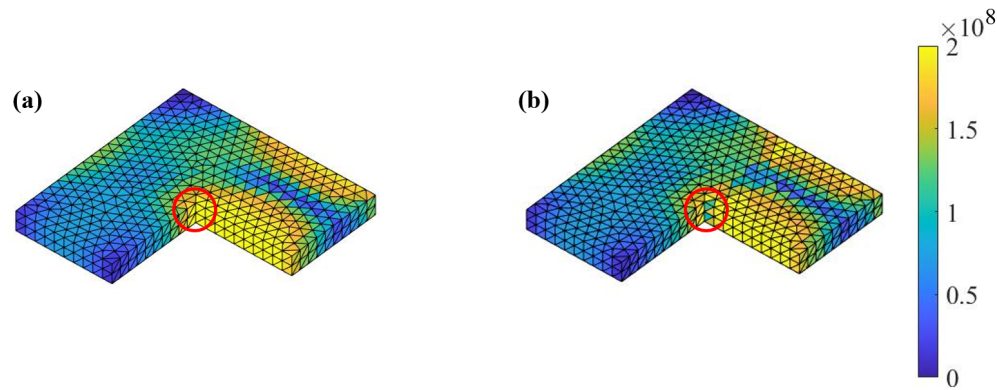


**Figure 12 Comparison of Von-Mises stress distributions in hardening simulation:** (a) The distribution of Von-Mises stresses (unit: Pa) by FE-ROM; and (d) Von-Mises stresses by the proposed FE-RNN.



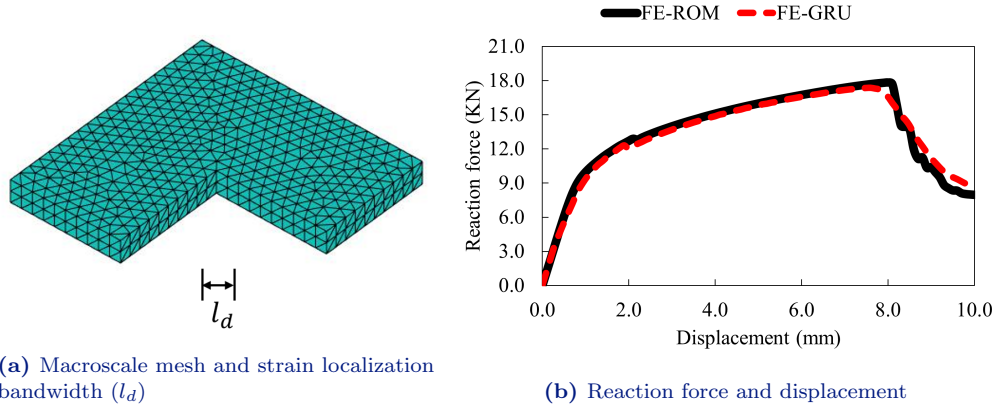


**Figure 13 Damage simulations of the L-shape bracket:** (a) The macroscale discretization and strain localization bandwidth applied in the damage function; and (b) Comparison of the softening load-displacement curves between FE-ROM and FE-RNN.

bandwidth  $l_d = 15$  mm whose length comparison to the mesh size of the bracket is illustrated in the Figure 13(a). The force-displacement curves are compared in 13(b) where the general trends of the two methods match well especially for the hardening section. Minor discrepancy manifests in the softening regime where the data-driven model tends to break at a slightly smaller boundary condition value and underestimate the load-carrying capacity by about 2.5%. The underlying reason could be due to the fact that material softening behaviors dramatically increase the complexity of the governing functions which it becomes increasingly hard for our RNN surrogate to match with.

We further compare the distributions of damage variables and Von-Mises stresses at the boundary condition of  $d = 10$  mm in Figures 14 and 15, respectively. Both field variables' distributions see good agreements between the two approaches. In Figure 14, we observe fracture bands initiate from the sharp corner and stretch towards the right rim. We can also clearly see the effects of imposing non-local damage functions in avoiding non-physical single-layer fracture bands. As for the stress distributions in Figure 15, both approaches indicate that the local stress values are significantly reduced within fracture bands indicating a loss of load-carrying capacity in the fractured elements. We note minor discrepancy of local stresses at the front tip of the fracture bands between the two methods: while the mechanistic model (FE-ROM) indicates relatively low stresses at the highlighted region, the data-driven model (FE-RNN) suggests stress concentrations which would trigger damage if the component is further deformed. We note that such stress concentrations can be used to understand the reason why the data-driven model predicts an earlier damage occurrence than the benchmark in Figure 13(b).

The discrepancy between the proposed FE-RNN and benchmark can be further quantified by the histogram of errors as shown in Figure 16. In terms of damage variables, it is quite clear from Figure 16(a) that the two approaches yield identical solutions in the majority (more than 80%) of elements. Based on the distributions of stress errors in Figure 16(b), we can see relatively large errors in about 2% of all elements. It should be noted, however, for most elements, their absolute errors are smaller than about 10% between the two methods, indicating a good agreement.

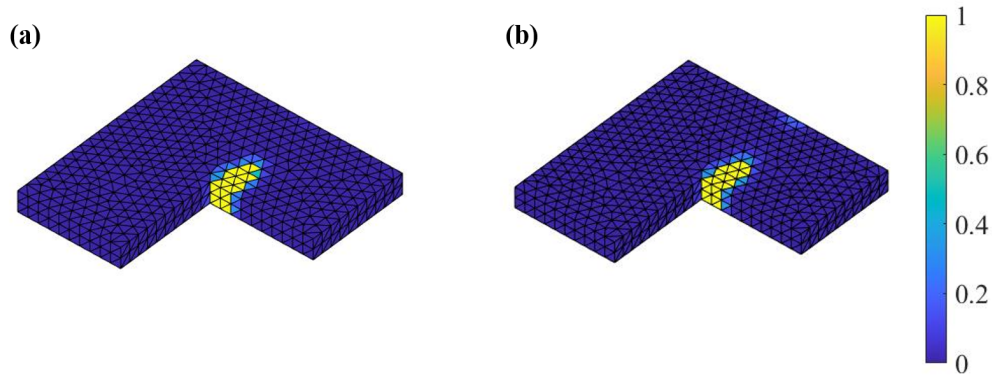


**Figure 14 Comparison of damage patterns:** (a) The distribution of damage variables by FE-ROM; and (d) Damage variables via FE-RNN. Color yellow indicates a full material fracture while blue represents an intact state.

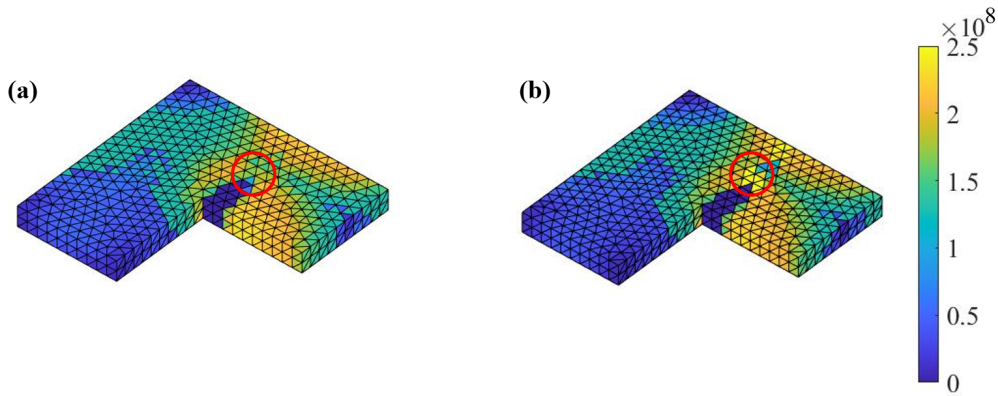


**Figure 15 Comparison of Von-Mises stress distributions in softening simulation:** (a) The distribution of Von-Mises stresses (unit: Pa) by FE-ROM; and (d) Von-Mises stresses by FE-RNN.

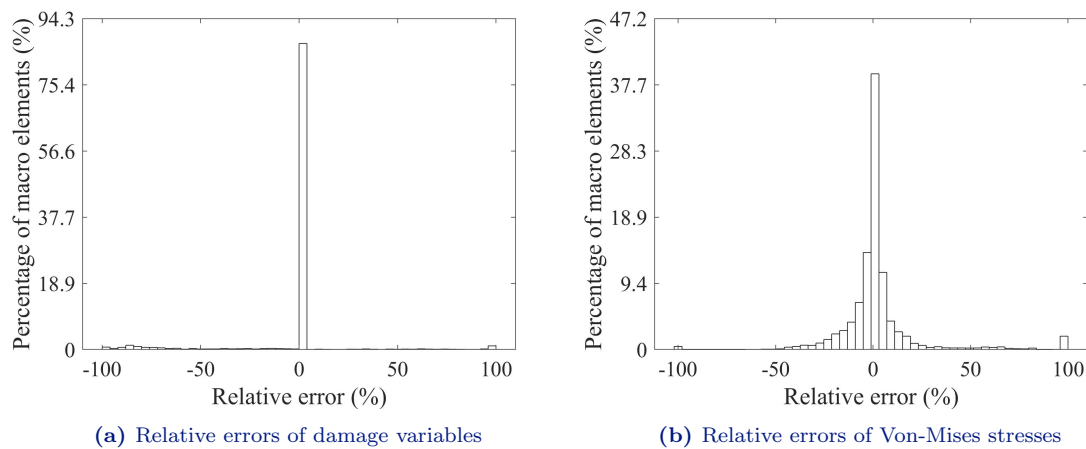


**Figure 16 Histogram of relative errors of field variables:** (a) Relative errors of the values of damage variables in Figure 14; and (b) Relative errors of the values of Von-Mises stresses in Figure 15.

**Table 1 Breakdown of computational time of the L-shape bracket model:** Despite considerable costs in database generation and training of the RNN, its efficiency (measured by clock time) in the multiscale simulations is about  $125\times$  and  $1240\times$  higher than ROM and  $FE^2$ , respectively, where the time estimation of  $FE^2$  comes from the time comparison in Figure A.3(b).

	FE-RNN	FE-ROM	$FE^2$ (estimation)
Database generation	$239.5 \times 60$ CPU-hour	-	-
RNN training	$4.3 \times 2$ GPU-hour	-	-
Multiscale simulation	$0.4 \times 4$ CPU-hour	$49.8 \times 60$ CPU-hour	$494.0 \times 60$ CPU-hour

In order to quantify computational costs, we break down the computational costs of different steps in this multiscale model as shown in Table 1. Comparing to the mechanistic multiscale models (FE-ROM and  $FE^2$ ), our data-driven model (FE-RNN) requires additional costs on database generation and model training. Even though substantially expensive, such two steps only need to be performed once, and the trained RNN model can be deployed at any multiscale simulations without extra costs. In terms of the online clock time, our RNN-based multiscale model shows superior efficiency to the mechanics models (FE-ROM and  $FE^2$ ) with about  $125\times$  and  $1240\times$  accelerations, respectively. It is noted we do not directly perform the  $FE^2$  due to its prohibitively demanding costs, its computational time is estimated by comparing to the ROM on a smaller multiscale simulation whose time comparison is shown in Appendix A in Figure A.3. We also note that while the training procedure is performed by two GPU processors, both the database generation of the FE-RNN and multiscale simulations of FE-ROM and  $FE^2$  are carried out by paralleling 60 CPU cores with 360 GB RAM on a HPC. Comparatively, the proposed RNN model only needs four CPU cores on a modest desktop for the multiscale computation, providing feasible analysis solutions to engineers without accessibility to large computational resources.

### 4.3 Mesh convergence study

One of the major challenges of using continuum mechanics to simulate softening behaviors is to prevent fracture bands residing in single element wide layers. One popular solution is to apply non-local functions to constrain damage patterns at different discretization levels. To this end, we apply the proposed RNN model to a new 3D model in this section, and assess its robustness through a mesh convergence study on damage behaviors.

The geometry, dimensions and boundary conditions of the double notched specimen is demonstrated in Figure 17(a). The specimen is fully fixed at the left surface, and its right surface is subject to an extension with a displacement boundary condition of  $d = 0.6$  mm. In this experiment, the whole specimen is assumed as the multiscale domain where each IP is associated with one porous RVE. For the mesh convergence study, we discretize the specimen with three different mesh sizes: a coarse mesh with 7,000 elements, a medium mesh with 18,000 elements, and a fine mesh with 28,000 elements.

We demonstrate the reaction force-displacement curves as in Figure 17(b). From the figure, we notice that the three mesh levels achieve very close elasto-plastic hardening responses, but are slightly different in the softening regime. Specifically, we note that with the spatial discretization increasing from medium to fine level, the post-failure force-displacement responses tend to converge.

**Table 2 Computational time of the double notched model:** The multiscale simulations of the double notched specimen are performed by the proposed FE-RNN model on a modest desktop with four CPU cores where the computational costs of one-time data generation and model training are reported in Table 1.

Number of macro-elements	Multiscale simulation time
7,000	$3.1 \times 4$ CPU-hour
18,000	$7.5 \times 4$ CPU-hour
28,000	$10.5 \times 4$ CPU-hour

The convergence can be also observed by inspecting the stress distributions and damage patterns from Figure 18 with the displacement boundary condition of  $d = 0.6$  mm. On the one hand, from Figure 18(a) and (b), we can clearly see that at all mesh levels, the damage initiates at the inner circular surfaces and propagates across the specimen as being further loaded. The influence of imposing non-local function is evident: it not only successfully avoids non-physical single-element-wide damage layers, but also constrains the fracture bandwidth regardless of the mesh sizes. On the other hand, with finer mesh, stress distributions are more alike with stress concentrations at both fracture front tips and around sharp corners.

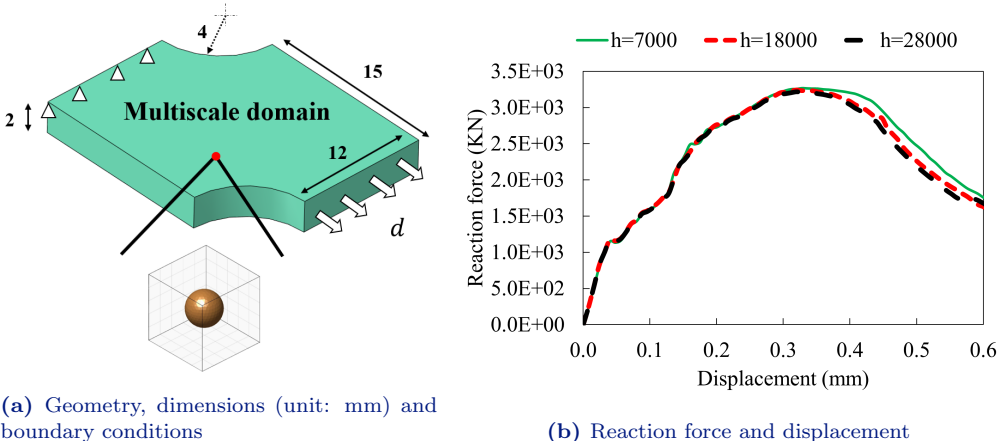
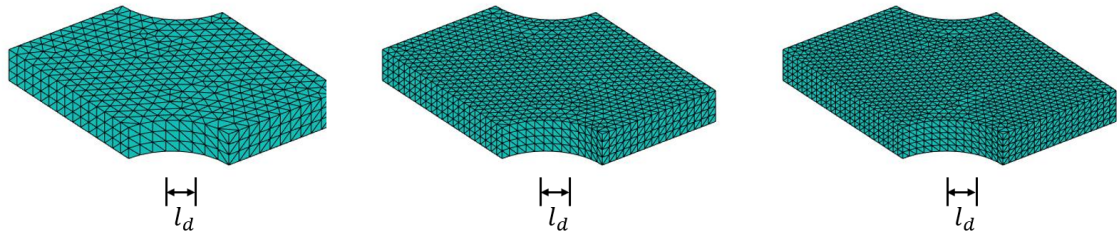


**Figure 17 Multiscale model of double-notched specimen:** (a) Every macroscale integration point is associated with a microscale porous RVE; and (b) Convergence study of the softening load-displacement curves with different macro discretization levels.

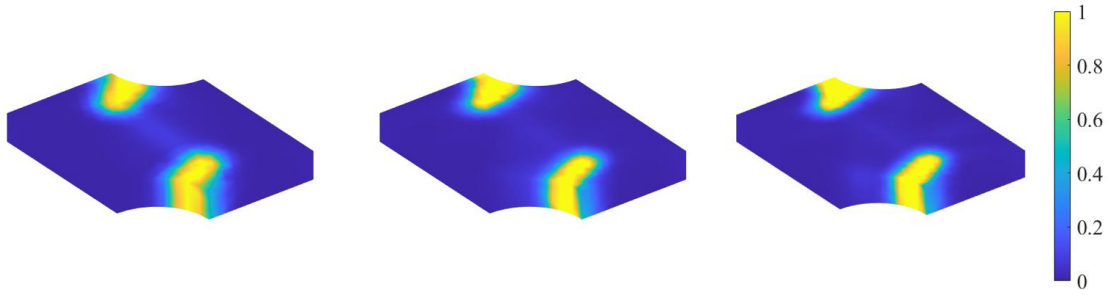
We report the simulation time of this multiscale double notched specimen in Table 2. We emphasize that due to the superior efficiency, our trained FE-RNN can be applied to any multiscale models with no extra costs of data generation and model training. In specific, the trained FE-RNN mode is so lightweight that it can run on a regular desktop with four CPU cores and 16GB RAM. Base on the time comparison in Table 1, simulating the multiscale model with 28,000 elements would require the clock time of 1,304.8 hours (54.4 days) and 12,942.8 hours (539.3 days) by paralleling 60 CPU cores with 360 GB RAM for FE-ROM and FE<sup>2</sup>, respectively.

## 5 Conclusions

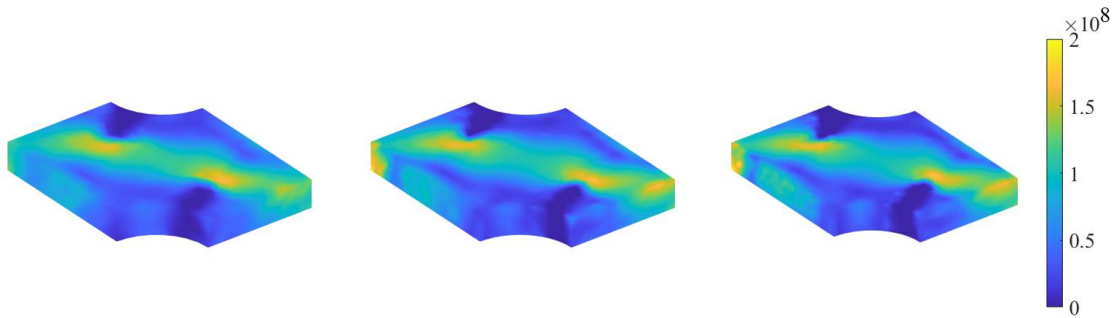
In this contribution, we propose a computational framework of a physics-constrained deep learning network for emulating the homogenized nonlinear path-dependent microstructural material behaviors in 3D large-scale multiscale simulations. Our deep learning model builds



(a) Mesh sizes and strain localization bandwidth ( $l_d$ )



(b) Damage patterns



(c) Von-Mises stress distributions

**Figure 18 Mesh convergence study of field variables by our FE-RNN:** With the increase of the number of macro-elements in (a), both the damage patterns in (b) and stress distributions in (c) show convergence.

on the RNN model which is trained on a database containing sequences of random microstructural deformation and responses. To reduce the computational costs of the database generation while preserving data generality, our sequential data is created by a GP-based DoE that is confined by prescribing material’s volume change to reduce the number of sampling deformation sequences. In addition, we adopt mechanistic ROM for the simulation of microstructural effective responses to reduce the computational cost per deformation sequence. Our database is created with 30,000 data sequences, while each sequence contains six random strain components and seven effective responses at each of the 100 loading steps, together accounting for a total of 39 million data points.

To facility the training and inference of our emulator on such a big data set, we modify RNN architecture by incorporating two physical constraints. The first constraint comes from thermodynamic-consistent microstructural energy analysis, and it is reinforced as a soft constraint by adding a penalty term to the loss function. The second constraint enforcing the irreversible nature of damage processes is implemented as a hard constraint by directly manipulating the temporal variation of our emulator’s outputs in a constrained RNN architecture.

The accuracy of our model is validated by comparing with the benchmark of microstructural effective responses that are unseen from the training process. Its accuracy is further verified in multiscale models that are subject to complex and cyclic loading conditions by providing quite close solutions to that of benchmark concurrent solver. We proceed to demonstrate that our surrogate model is robust enough to provide reliable multiscale softening solutions that are post-failure convergent and mesh independent.

Our experiments reveal that while the costs of database generation and model training are considerable, our trained emulator shows superior efficiency in online computations. For example, our data-driven model is about four orders of magnitude faster than classic FE<sup>2</sup> approach in terms of CPU hours. Such high efficiency makes our model promising for many computationally intensive tasks that would require large computational facilities (multi-core CPUs and GPUs) or need long simulation time.

Our framework can be extended to multiple directions in future work. First, minimization of inference error is critical especially for iterative solvers. While teacher-forcing mechanism [29] shows significant accuracy improvement in training process, we are interested in how its performance improvement can be translated in online iterative solution process lacking ground truth values. Second, we are also interested in studying the impacts of spatially varying material properties and microstructural morphology on components’ behaviors. However, adding such variations would dramatically increase the dimension of sampling space and therein the number of sampling points. In such scenario, to reduce sampling efforts, an adaptive sampling strategy [30] for sequence learners needs to be investigated. Last but not the least, our work can be potentially extended for studying uncertainty quantification [31] and design optimization for material and structural designs [32–35].

### **Declaration of competing interest**

The authors declare that they have no known competing financial interests or personal relationships that could have appeared to influence the work reported in this paper.

## Acknowledgments

The authors appreciate the supports from ACRC consortium members. The authors also thank Dr. Ling Wu and Dr. Ludovic Noels for helpful discussions and constructive suggestions. Ramin Bostanabad also acknowledges NSF funding (award number OAC-2103708).

## Appendices

### A Deflated clustering analysis

Simulation of microstructural softening via classic FE<sup>2</sup> method involves demanding computational costs, which is prohibitive for generating big training data for machine learning models. To accelerate the database generation, we adopt our previously developed mechanistic ROM, i.e., deflated clustering analysis (DCA) [5, 6]. Its high efficiency comes from two facts: (1) the number of unknown variables in the system is dramatically reduced from a large number of finite elements to a few clusters by agglomerating elements via clustering as shown in Figure A.1, and (2) the algebraic equations of the reduced system contains much fewer close-to-zero eigenvalues that results in better convergence comparing to the classic FE system.

Our DCA utilizes k-means clustering, i.e., an unsupervised machine learning technique for data interpretation and grouping, to agglomerate neighboring elements into a set of interactive irregular-shape clusters. The clustering begins with feeding the coordinates of element centroids into a feature space where randomly scattered cluster seeds serve as initial cluster means. Clusters accepts or rejects elements by iteratively minimizing the within-cluster variance until all elements are assigned to a cluster. The clustering procedure can be mathematically stated as a minimization problem as:

$$\mathbf{C} = \min_{\mathbf{C}} \sum_{I=1}^k \sum_{n \in C^I} \|\varphi_n - \bar{\varphi}_I\|^2 \quad (\text{A-1})$$

where  $\mathbf{C}$  represents the k clusters with  $\mathbf{C} = \{C^1, C^2, \dots, C^k\}$ .  $\varphi_n$  and  $\bar{\varphi}_I$  indicate the coordinates of the centroid of the  $n^{\text{th}}$  element and the mean of the coordinates of the  $I^{\text{th}}$  cluster, respectively. A clustering example is illustrated in Figure A.1 where the discrete domain of a 2D generic RVE with 5,000 elements are decomposed into 100 clusters.

We construct clustering-based reduced mesh via Delaunay triangularization by connecting cluster centroids where the topological relations between clusters are preserved from the original FE mesh. By assuming the motions of cluster centroids are directly related to clustering nodes, we can compute the nodal displacements via polynomial augmented radian point interpolation [36] as:

$$\mathbf{u}_c = \mathbf{R}\mathbf{a} + \mathbf{Z}\mathbf{b} \quad (\text{A-2})$$

where  $\mathbf{u}_c$  represent the displacements of cluster centroids.  $\mathbf{a}$  is the coefficient vector of the radial basis function matrix  $\mathbf{R}$ , and  $\mathbf{b}$  is the coefficient vector of the polynomial basis matrix  $\mathbf{Z}$ . Meanwhile, the radial coefficient and the polynomial basis need to satisfy the following equation for every node per cluster and every polynomial basis function to ensure solution

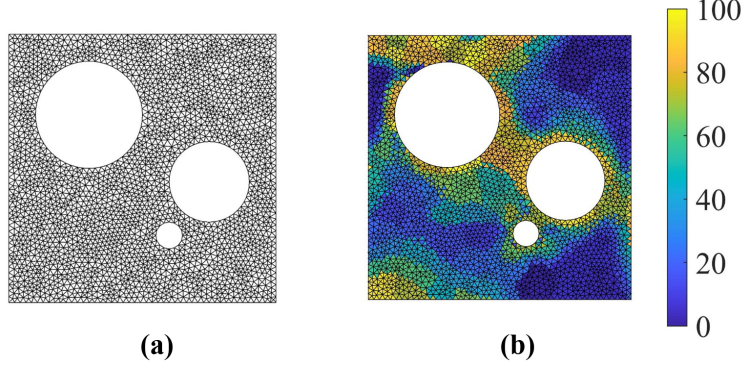


**Figure A.1 Demonstration of clustering in ROM:** The domain of a generic 2D RVE with 5,000 elements in (a) are decomposed into 100 clusters in (b) where elements in the same cluster are assigned with the same color.

uniqueness [36] as:

$$\mathbf{Z}\mathbf{a} = \mathbf{0} \quad (\text{A-3})$$

The displacements of cluster centroids are augmented with rotational degrees of freedom to represent the six rigid body motions in a 3D deflation space [37], including three translations and three rotations. Upon the completion of non-linear analysis on the reduced mesh, the displacement solutions can be projected back to the original FE mesh by:

$$\mathbf{u}_i^j = \mathbf{W}_i^j \boldsymbol{\lambda}_j \quad (\text{A-4})$$

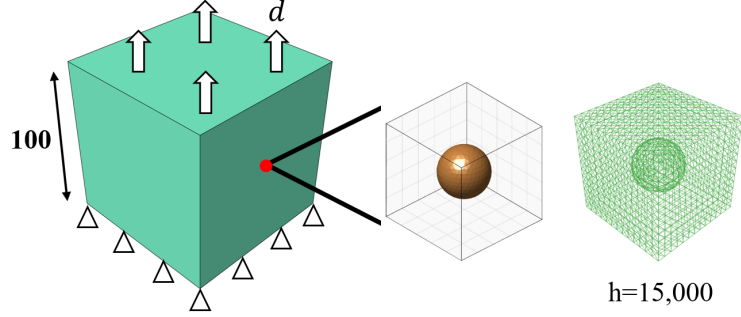
where  $\mathbf{u}_i^j$  represents the displacement vector at the  $i^{\text{th}}$  node in the  $j^{\text{th}}$  cluster. In addition,  $\boldsymbol{\lambda}_j$  is the rigid body motion of the centroid of the  $j^{\text{th}}$  cluster, while the  $\mathbf{W}_i^j$  indicates the deflation matrix for the  $i^{\text{th}}$  node in the  $j^{\text{th}}$  cluster as:

$$\boldsymbol{\lambda}_j = [u_{jx}, u_{jy}, u_{jz}, \theta_{jx}, \theta_{jy}, \theta_{jz}]^T; \quad \mathbf{W}_i^j = \begin{bmatrix} 1 & 0 & 0 & 0 & z_i^j & -y_i^j \\ 0 & 1 & 0 & -z_i^j & 0 & x_i^j \\ 0 & 0 & 1 & y_i^j & -x_i^j & 0 \end{bmatrix} \quad (\text{A-5})$$

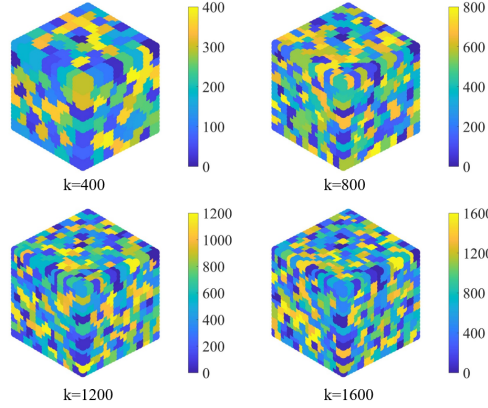
where  $u_{jx}$  and  $\theta_{jx}$  are the displacement and rotation of the  $j^{\text{th}}$  cluster along x axis, and the  $(x_i^j, y_i^j, z_i^j)$  are the relative 3D coordinates of the  $i^{\text{th}}$  node with respect to the centroid of the  $j^{\text{th}}$  cluster. By assuming all elements in the same cluster share identical stress and strain fields, microstructural effective responses can be reproduced in a highly efficient manner such that the unknown variables are dramatically decreased from FE system that accounts for distinct field variables per element to the reduced system with much fewer distinct solutions per cluster.

To demonstrate the efficacy of DCA-based ROM, we compare its simulation results on a 3D multiscale cube against the classic FE<sup>2</sup> method in Figure A.2. The macro-cube is fully constrained at its bottom surface, and it is subject to an upward extension on the top surface with  $d = 7$  mm. The cube is meshed with 12 tetrahedral elements of reduced-integration (one IP at the center of each tetrahedron). We assume each macro-IP is associated with the





(a) Geometry, dimensions (unit: mm), and boundary conditions of the macro-model; Geometry and the finite element mesh of the porous RVE



(b) RVE clustering

**Figure A.2 Multiscale cube model:** (a) Every integration point of the macro-cube model is associated with a porous RVE; and (b) The RVE domain is discretized by different numbers of clusters.

same porous RVE containing one spherical pore in the middle as shown in Figure A.2(a). To illustrate the effects of clustering on the RVE’s effective softening behaviors, we adopt four clustering levels on the same RVE mesh (15,000 elements) with the number of clusters ( $k$ ) as 400, 800, 1,200 and 1,600 as in the Figure A.2(b).

We compare the reaction force-displacement curves from  $FE^2$  and FE-ROM in Figure A.3(a). By considering the  $FE^2$  solutions as the benchmark, we observe that: (1) the FE-ROM solutions of  $k = 400$  generally overestimates the component’s strength which is due to insufficient clustering in the RVE that results in artificially strong material responses as discussed in [3, 5]; and (2) With more clusters, the FE-ROM responses, especially the post-failure behaviors, become more and more closer to the benchmark. In specific, we observe that when the numbers of clusters increase to 1,200 and 1,600, FE-ROMs achieve sufficiently accurate results compared to  $FE^2$  benchmark.

We further quantify the computational costs of the different solvers in Figure A.3(b). While all experiments are performed on a HPC by paralleling 60 CPU cores with 360 GB RAM, the clock time of  $FE^2$  is the longest, accounting for 24.9 hours. The clock time of the ROM with 1,200 and 1,600 clusters is about 2.5 and 3.2 hours, resulting in the acceleration factors of 9.9 and 7.8, respectively. Considering the fact that the ROM of  $k = 1,200$  is about 28% faster than its counterpart of  $k = 1,600$  while achieving similar accuracy, we adopt  $k = 1,200$  as the clustering of choice for the generation of the RVE softening database

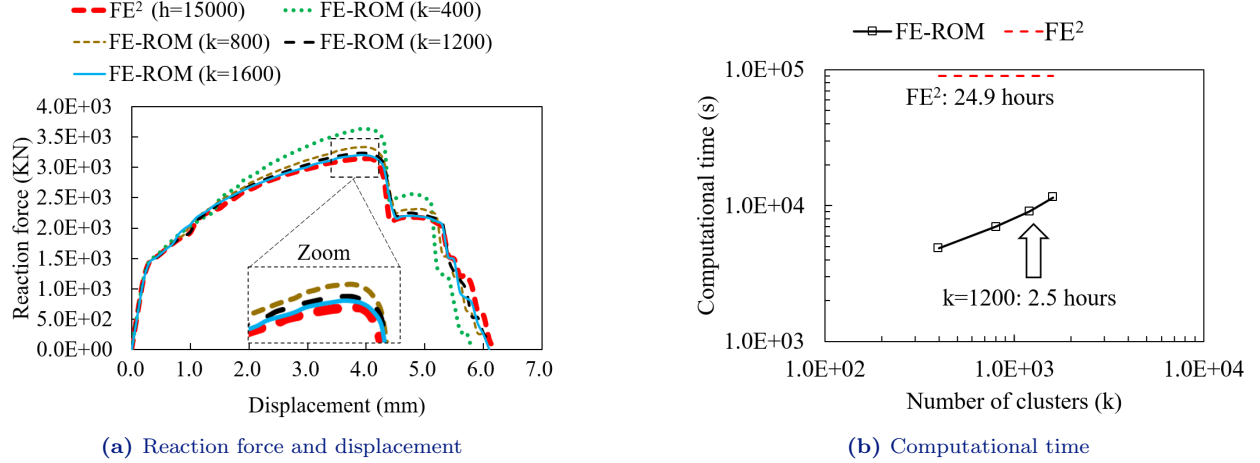


**Figure A.3 Results of the multiscale cube model:** (a) Comparison of the softening load-displacement curves between FE<sup>2</sup> and FE-ROM with different clusters; and (b) Comparison of computational time.

and for the FE-ROM multiscale simulations in Section 4.

## B Gated recurrent unit

In order to avoid the vanishing and exploding gradient issues of traditional RNN in processing long sequential data, more advanced memory cells are developed for sequential learners, including the long short term memory (LSTM) and the gated recurrent unit (GRU). Specifically, GRU is a variant of the LSTM, showing comparable performance to LSTM while exhibiting higher efficiency due to its compacted internal structures and fewer math operations. It is for this reason we choose GRU as the memory cell in our proposed RNN architecture as in Figure 6.

To demonstrate the working mechanism, we illustrate a GRU layer of three interconnected cells in Figure B.1. In a GRU layer, a typical cell at an arbitrary time step  $t$  generates predictions  $\hat{\mathbf{y}}_t$  and internal memory-like hidden variables  $\mathbf{h}_t$  after reading in the current inputs  $\mathbf{x}_t$  and the hidden variables  $\mathbf{h}_{t-1}$  from the previous cell. Comparing to the RNN cell in Figure 5(b), the GRU cell has a more sophisticated gate structure to regulate its internal information flow. Specifically, a GRU cell includes two gate operations: a reset gate and an update gate.

The reset gate  $\mathbf{r}_t$  begins to read the current input state  $\mathbf{x}_t$  and the previous hidden state  $\mathbf{h}_{t-1}$ . It proceeds to determine a candidate hidden state  $\tilde{\mathbf{h}}_t$  by filtering out less important information passing from the previous cell. Its operations include:

$$\mathbf{r}_t = \sigma(\mathbf{W}_{hr}\mathbf{h}_{t-1} + \mathbf{W}_{xr}\mathbf{x}_t + \mathbf{b}_r) \quad (\text{B-1a})$$

$$\tilde{\mathbf{h}}_t = \tanh(\mathbf{r}_t \odot \mathbf{W}_{h\tilde{h}}\mathbf{h}_{t-1} + \mathbf{W}_{x\tilde{h}}\mathbf{x}_t + \mathbf{b}_{\tilde{h}}) \quad (\text{B-1b})$$

where  $\sigma$  is the sigmoid activation function that returns a value in the range of  $[0, 1]$ ,  $\tanh$  is the hyperbolic tangent function, and  $\odot$  represents the element-wise product operation.  $\mathbf{W}_{hr}$ ,  $\mathbf{W}_{xr}$ ,  $\mathbf{W}_{h\tilde{h}}$ ,  $\mathbf{W}_{x\tilde{h}}$  are the weighting matrices associated with the hidden state, the input state, the hidden-to-candidate hidden state and the input-to-candidate hidden state, respectively.  $\mathbf{b}_r$  and  $\mathbf{b}_{\tilde{h}}$  are the biases applied to the sigmoid function in the reset gate and the hyperbolic tangent function, respectively.

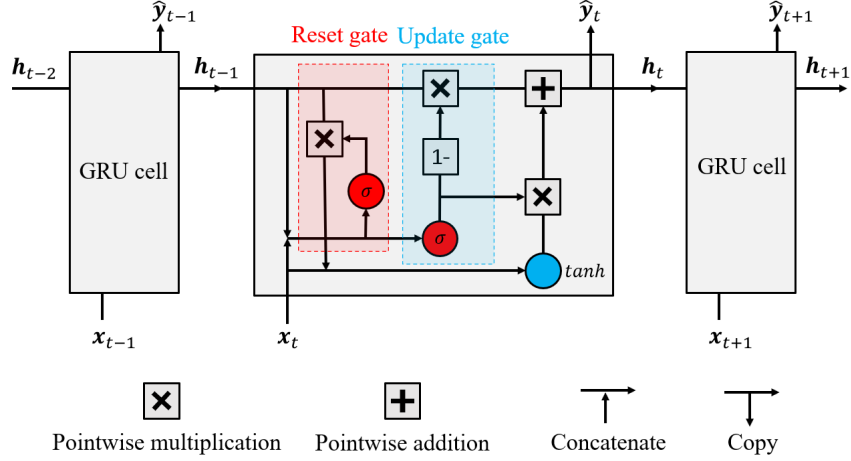


**Figure B.1 Architectures of GRU layer and cells:** The internal structure and mathematical operations are demonstrated in the GRU cell at time step  $t$ .

In a similar manner, the update gate operates on  $\mathbf{x}_t$  and  $\mathbf{h}_{t-1}$  but using different weights and biases terms. More precisely, the update gate linearly interpolates the previous hidden state  $\mathbf{h}_{t-1}$  and the candidate hidden state  $\tilde{\mathbf{h}}_t$  to update the memory-like hidden state  $\mathbf{h}_t$  passing onto the next time step:

$$\mathbf{u}_t = \sigma(\mathbf{W}_{hu}\mathbf{h}_{t-1} + \mathbf{W}_{xu}\mathbf{x}_t + \mathbf{b}_u) \quad (\text{B-2a})$$

$$\mathbf{h}_t = \mathbf{u}_t \odot \mathbf{h}_{t-1} + (1 - \mathbf{u}_t) \odot \tilde{\mathbf{h}}_t + \mathbf{b}_h \quad (\text{B-2b})$$

where  $\mathbf{W}_{hu}$  and  $\mathbf{W}_{xu}$  are the weights applied onto the hidden state and input state in the update gate.  $\mathbf{b}_u$  and  $\mathbf{b}_h$  are the two biases associated to the sigmoid function and the generation of current hidden state. In the end, the cell output at the current time step  $\hat{\mathbf{y}}_t$  is linearly transformed from the hidden state as:

$$\hat{\mathbf{y}}_t = \mathbf{W}_{hy}\mathbf{h}_t + \mathbf{b}_y \quad (\text{B-3})$$

where  $\mathbf{W}_{hy}$  and  $\mathbf{b}_y$  are the weights and biases associated to the current output state  $\hat{\mathbf{y}}_t$ . We note that all the weights and biases of the GRU networks are iteratively updated through BPTT during training.

## References

- [1] George J Dvorak. “Transformation field analysis of inelastic composite materials”. In: *Proceedings of the Royal Society of London. Series A: Mathematical and Physical Sciences* 437.1900 (1992), pp. 311–327.
- [2] Sophie Roussette, Jean-Claude Michel, and Pierre Suquet. “Nonuniform transformation field analysis of elastic–viscoplastic composites”. In: *Composites Science and Technology* 69.1 (2009), pp. 22–27.
- [3] Zeliang Liu, MA Bessa, and Wing Kam Liu. “Self-consistent clustering analysis: an efficient multi-scale scheme for inelastic heterogeneous materials”. In: *Computer Methods in Applied Mechanics and Engineering* 306 (2016), pp. 319–341.
- [4] Shaoqiang Tang, Lei Zhang, and Wing Kam Liu. “From virtual clustering analysis to self-consistent clustering analysis: a mathematical study”. In: *Computational Mechanics* 62.6 (2018), pp. 1443–1460.
- [5] Shiguang Deng, Carl Soderhjelm, Diran Apelian, and Ramin Bostanabad. “Reduced-order multiscale modeling of plastic deformations in 3D alloys with spatially varying porosity by deflated clustering analysis”. In: *Computational Mechanics* 70.3 (2022), pp. 517–548.
- [6] Shiguang Deng, Diran Apelian, and Ramin Bostanabad. “Concurrent Multiscale Damage Analysis with Adaptive Spatiotemporal Dimension Reduction”. In: *arXiv preprint arXiv:2205.12149* (2022).
- [7] M Mozaffar, R Bostanabad, W Chen, K Ehmann, Jian Cao, and MA Bessa. “Deep learning predicts path-dependent plasticity”. In: *Proceedings of the National Academy of Sciences* 116.52 (2019), pp. 26414–26420.
- [8] Kun Wang and WaiChing Sun. “A multiscale multi-permeability poroplasticity model linked by recursive homogenizations and deep learning”. In: *Computer Methods in Applied Mechanics and Engineering* 334 (2018), pp. 337–380.

- [9] Ling Wu, Nanda Gopala Kilingar, Ludovic Noels, et al. “A recurrent neural network-accelerated multi-scale model for elasto-plastic heterogeneous materials subjected to random cyclic and non-proportional loading paths”. In: *Computer Methods in Applied Mechanics and Engineering* 369 (2020), p. 113234.
- [10] F Ghavamian and A Simone. “Accelerating multiscale finite element simulations of history-dependent materials using a recurrent neural network”. In: *Computer Methods in Applied Mechanics and Engineering* 357 (2019), p. 112594.
- [11] Hernan J Logarzo, German Capuano, and Julian J Rimoli. “Smart constitutive laws: Inelastic homogenization through machine learning”. In: *Computer methods in applied mechanics and engineering* 373 (2021), p. 113482.
- [12] Fermin Otero, Sergio Oller, and Xavier Martinez. “Multiscale computational homogenization: review and proposal of a new enhanced-first-order method”. In: *Archives of Computational Methods in Engineering* 25.2 (2018), pp. 479–505.
- [13] Zdenek P Bazant. “Can multiscale-multiphysics methods predict softening damage and structural failure?” In: *International Journal for Multiscale Computational Engineering* 8.1 (2010).
- [14] Zeliang Liu, Mark Fleming, and Wing Kam Liu. “Microstructural material database for self-consistent clustering analysis of elastoplastic strain softening materials”. In: *Computer Methods in Applied Mechanics and Engineering* 330 (2018), pp. 547–577.
- [15] Michael Smith. “ABAQUS Standard User’s Manual”. In: *Dassault Systèmes Simulia Corp* (2009), Version 6.9.
- [16] Javier Oliver, Alfredo Edmundo Huespe, and JC Cante. “An implicit/explicit integration scheme to increase computability of non-linear material and contact/friction problems”. In: *Computer Methods in Applied Mechanics and Engineering* 197.21-24 (2008), pp. 1865–1889.
- [17] Miroslav Silhavy. *The mechanics and thermodynamics of continuous media*. Springer Science & Business Media, 2013.

- [18] Han Yang, Sumeet Kumar Sinha, Yuan Feng, David B McCallen, and Boris Jeremić. “Energy dissipation analysis of elastic–plastic materials”. In: *Computer Methods in Applied Mechanics and Engineering* 331 (2018), pp. 309–326.
- [19] Heidi P Feigenbaum and Yannis F Dafalias. “Directional distortional hardening in metal plasticity within thermodynamics”. In: *International Journal of Solids and Structures* 44.22-23 (2007), pp. 7526–7542.
- [20] Kurt Hornik, Maxwell Stinchcombe, and Halbert White. “Multilayer feedforward networks are universal approximators”. In: *Neural networks* 2.5 (1989), pp. 359–366.
- [21] Ridha Hambli, Houda Katerchi, and Claude-Laurent Benhamou. “Multiscale methodology for bone remodelling simulation using coupled finite element and neural network computation”. In: *Biomechanics and modeling in mechanobiology* 10.1 (2011), pp. 133–145.
- [22] Jean-Louis Chaboche. “Continuous damage mechanics—a tool to describe phenomena before crack initiation”. In: *Nuclear engineering and design* 64.2 (1981), pp. 233–247.
- [23] Xiaoxin Lu, Dimitris G Giovanis, Julien Yvonnet, Vissarion Papadopoulos, Fabrice Detrez, and Jinbo Bai. “A data-driven computational homogenization method based on neural networks for the nonlinear anisotropic electrical response of graphene/polymer nanocomposites”. In: *Computational Mechanics* 64.2 (2019), pp. 307–321.
- [24] Zachary C Lipton, John Berkowitz, and Charles Elkan. “A critical review of recurrent neural networks for sequence learning”. In: *arXiv preprint arXiv:1506.00019* (2015).
- [25] Boris Hanin. “Which neural net architectures give rise to exploding and vanishing gradients?” In: *Advances in neural information processing systems* 31 (2018).
- [26] Ralf C Staudemeyer and Eric Rothstein Morris. “Understanding LSTM—a tutorial into long short-term memory recurrent neural networks”. In: *arXiv preprint arXiv:1909.09586* (2019).
- [27] Andrej Karpathy, Justin Johnson, and Li Fei-Fei. “Visualizing and understanding recurrent networks”. In: *arXiv preprint arXiv:1506.02078* (2015).

- [28] Pablo Márquez-Neila, Mathieu Salzmann, and Pascal Fua. “Imposing hard constraints on deep networks: Promises and limitations”. In: *arXiv preprint arXiv:1706.02025* (2017).
- [29] Alex M Lamb, Anirudh Goyal ALIAS PARTH GOYAL, Ying Zhang, Saizheng Zhang, Aaron C Courville, and Yoshua Bengio. “Professor forcing: A new algorithm for training recurrent networks”. In: *Advances in neural information processing systems* 29 (2016).
- [30] Samy Bengio, Oriol Vinyals, Navdeep Jaitly, and Noam Shazeer. “Scheduled sampling for sequence prediction with recurrent neural networks”. In: *Advances in neural information processing systems* 28 (2015).
- [31] Ramin Bostanabad, Biao Liang, Jiaying Gao, Wing Kam Liu, Jian Cao, Danielle Zeng, Xuming Su, Hongyi Xu, Yang Li, and Wei Chen. “Uncertainty quantification in multiscale simulation of woven fiber composites”. In: *Computer Methods in Applied Mechanics and Engineering* 338 (2018), pp. 506–532.
- [32] Mikhail Osanov and James K Guest. “Topology optimization for architected materials design”. In: *Annual Review of Materials Research* 46 (2016), pp. 211–233.
- [33] Zheng-Dong Ma, Noboru Kikuchi, Christophe Pierre, and Basavaraju Raju. “Multidomain topology optimization for structural and material designs”. In: (2006).
- [34] Shiguang Deng and Krishnan Suresh. “Multi-constrained 3D topology optimization via augmented topological level-set”. In: *Computers & Structures* 170 (2016), pp. 1–12.
- [35] Shiguang Deng and Krishnan Suresh. “Multi-constrained topology optimization via the topological sensitivity”. In: *Structural and Multidisciplinary Optimization* 51.5 (2015), pp. 987–1001.
- [36] Gui-Rong Liu. *Meshfree methods: moving beyond the finite element method*. CRC press, 2009.

- [37] TB Jönsthövel, MB Van Gijzen, C Vuik, C Kasbergen, and A Scarpas. “Preconditioned conjugate gradient method enhanced by deflation of rigid body modes applied to composite materials”. In: *Computer Modeling in Engineering and Sciences (CMES)* 47.2 (2009), p. 97.